

1

Revised Manuscript (Revision 2)

2

Estimation of radiation damage in titanites using Raman spectroscopy

3 Beatrix Muriel Heller^{1,ab}, Nils Keno Lünsdorf¹, István Dunkl¹, Ferenc Molnár², Hilmar von
4 Eynatten¹

5 ¹Geoscience Center, Sedimentology and Environmental Geology, University of Göttingen,
6 Goldschmidtstraße 3, 37077 Göttingen, Germany

7 ²Geological Survey of Finland, P.O. Box 96, FI-02151 Espoo, Finland

8

Abstract

9 Recent studies have shown that α -damage in titanite influences He diffusivity and
10 thus the closure temperature of the (U-Th)/He system in titanite. We compare
11 different methods for measuring the α -dose in titanite by Raman spectroscopy.
12 293 Raman spectra of randomly oriented titanite fragments from the Archean
13 Karelian domain in eastern Finland along with some well-studied young titanites
14 and U-Pb standard reference materials were analyzed and related to the
15 concentration of α -emitting elements (U and Th) that generated damage in the
16 respective grains. Automated curve-fitting was performed by the IFORS software
17 and different curve-fitting protocols were tested and compared.

^acorrespondence: b-m.heller@gmx.de

^bcurrent address: GEOPS, Université Paris-Sud 11, Université Paris-Saclay, Bât. 504, F-91405 Orsay cedex, France

18 The Raman bands at 424 cm^{-1} and 465 cm^{-1} show a good correlation of full width
19 at half maximum (FWHM) and position with the α -dose. However, these bands
20 are not always present because titanite is highly anisotropic implying that Raman
21 spectra are sensitive to orientation. The intensity-weighted mean FWHM (iw-
22 FWHM) of all Raman bands of a spectrum proves to be the most robust measure
23 of the α -dose. A simplified fitting approach considering 15 peaks is sufficient to
24 describe the accumulated α -dose. For α -doses below $5 \times 10^{16}\alpha/\text{g}$ the iw-FWHM
25 is independent of α -dose and ranges from 25 to 50 cm^{-1} . Above this value the iw-
26 FWHM increases linearly with increasing α -dose up to $3 \times 10^{18}\alpha/\text{g}$. The linear
27 correlation can be described as $\text{iw-FWHM}[\text{cm}^{-1}] \sim 39(\pm 1.2)[\text{cm}^{-1}] + 3.84(+0.61, -$
28 $0.26) \times 10^{-17}[\text{cm}^{-1}/(\alpha/\text{g})] \times \alpha\text{-dose}[\alpha/\text{g}]$. The approach provides a pre-selection
29 method in order to optimize the range of α -doses of titanite crystals to be dated by
30 (U-Th)/He thermochronology.

31 keywords: titanite; (U-Th)/He; metamictization; radiation damage; α -dose;
32 Raman spectroscopy; thermochronology

33 **Introduction**

34 Low-T thermochronology is a widely-applied tool for deciphering thermal histories of cratonic
35 areas, especially when sedimentary successions constraining the timing of subsidence and
36 exhumation are missing. In contrast to zircon which has commonly effective uranium content
37 ($eU = U[\text{ppm}] + 0.235\text{Th}[\text{ppm}]$) of $\geq 300\text{ ppm}$ (up to 5000 ppm), titanite has usually lower eU
38 contents in the range of $10\text{--}500\text{ ppm}$ and is thus less subjected to metamictization. Moreover,
39 titanite is common in intermediate to mafic rocks where zircon is typically absent.

40 The closure temperature (T_c) of the (U–Th)/He thermochronometers is influenced by the
41 composition and crystalline state of the dated crystals. Among all influencing parameters
42 metamictization is the dominant one (Flowers 2009; Orme et al. 2016; Johnson et al. 2017). The
43 influence of metamictization on the T_c 's of the most widely used minerals, zircon and apatite, has
44 been intensively investigated (Shuster et al. 2006; Flowers et al. 2009; Gautheron et al. 2009;
45 Guenther et al. 2013; Orme et al. 2016). In contrast, its influence on the titanite (U–Th)/He
46 thermochronometer (THe) has been reported only recently (Baughman et al. 2017; Guenther et
47 al. 2017). These studies show that with increasing α -dose the T_c of the THe system drops to a
48 significantly lower value. Unfortunately, several aspects of the THe system remain unclear
49 (Reiners and Farley 1999; Stockli and Farley 2004; Cherniak and Watson 2011). Titanite has
50 been discussed as host material for nuclear waste (Weber et al. 1998; Stefanovsky et al. 2004;
51 Lumpkin 2006) and various studies focus on the effects of radiation damage in this mineral
52 (Bismayer et al. 2010; Salje et al. 2011; Beirau et al. 2016).

53 The α -dose of zircon can be estimated from the width of its main Raman band at approximately
54 $1000\text{--}1008\text{ cm}^{-1}$ (Zhang et al. 2000; Nasdala et al. 2001; Palenik et al. 2003; Nasdala et al. 2004).
55 Therefore, Raman spectroscopy offers a quick, non-destructive method for selecting grains for
56 zircon (U–Th)/He (ZHe) thermochronology according to their α -dose (e.g. Ault et al. 2018). For
57 titanite, as for zircon, metamictization affects the Raman spectrum by broadening and shifting the
58 position of several bands (Salje et al. 1993; Meyer et al. 1996; Zhang and Salje 2003; Bismayer
59 et al. 2010; Beirau et al. 2012; Zhang et al. 2013). However, Raman spectroscopy of titanite is
60 more complicated when compared to zircon because of (i) strong anisotropy, (ii) higher amount
61 of Raman bands, and (iii) adjacent Raman bands often overlap in highly metamict titanite grains
62 (e.g. Beirau et al. 2012; Zhang et al. 2013). Moreover, titanite crystals usually have irregular

63 shapes. Therefore mineral fragments without crystal faces are typically used for The dating,
64 which makes crystallographic orientation of the grains difficult.

65 So far, no advanced diffusion model exists for titanite that takes radiation damage into
66 consideration. As a consequence, The ages measured on highly damaged grains are more
67 difficult to interpret than The ages of slightly damaged grains. Therefore, the routine application
68 of The thermochronology requires an easy-to-use, orientation independent method for damage
69 estimation and selection of the crystals to be dated.

70 This study compares different approaches considering single peaks as well as the entire Raman
71 spectrum for quantifying the α -dose in titanite. We present coupled Raman, eU, and The data of
72 titanite from the Archean Karelian domain in Fennoscandia. The area has been tectonically stable
73 since the Svecofennian orogeny (approx. 1.92–1.80 Ga) (Kähkönen 2005; Lahtinen et al. 2005;
74 Heller et al., in prep) and since then all samples have experienced the same thermal history. To
75 cover a broad range of α -doses, measurements of younger titanite samples and titanite reference
76 materials with known age and simple cooling histories complement the dataset. The main goal of
77 this study is to establish a quick (and non-destructive) method for estimating the α -dose from the
78 titanite Raman spectrum. We demonstrate that characterization of the entire Raman spectrum can
79 be used as a robust estimator independent of grain orientation and evaluation method.

80 **Background**

81 **Crystal structure and metamictization of titanite**

82 Titanite, $\text{CaTi}(\text{SiO}_4)(\text{O}, \text{OH}, \text{F})$, also called sphene, is a monoclinic nesosilicate. Zig-zag chains
83 of corner-sharing TiO_6 octahedra are cross-linked by isolated SiO_4 -tetrahedra, building a
84 framework. This $(\text{TiOSiO}_4)_2$ -framework contains large cavities which enclose sevenfold-

85 coordinated Ca atoms (Speer and Gibbs 1976). Through lattice substitutions, titanite can
86 incorporate significant amounts of rare earth elements (REE), U, Th, Sr, Y, Mn and Pb at the
87 sevenfold Ca sites and at the octahedral Ti sites (Higgins and Ribbe 1976; Tiepolo et al. 2002;
88 Xu et al. 2015) and may also concentrate significant amounts of HFSEs, such as Nb, Ta, Zr and
89 W, on the octahedral Ti site (Groat et al. 1985; Lucassen et al. 2011).

90 The consecutive radioactive decay of U and Th atoms induces metamictization in titanite crystals
91 (Zhang and Salje 2003; Beirau et al. 2010; Bismayer et al. 2010; Beirau et al. 2012; Zhang et al.
92 2013; Beirau et al. 2014, 2016). In metamict titanites both crystalline and amorphous domains
93 coexist (Hawthorne et al. 1991; Lumpkin et al. 1991). Hawthorne et al. (1991) and Farges (1997)
94 suggest that metamictization leads to disordering around the Ti positions and a partial reduction
95 of the Ti coordination down to five and / or four. This further disturbs the Ti–O–Ti intra–chain
96 linkages (Beirau et al. 2012), triggering an anisotropic response of the titanite lattice. This means
97 that the plane containing Si-O-Ti-O bond closed contours is less susceptible to a self–
98 accumulation of defects as compared to the perpendicular planes, which contain chains of Ti-O
99 bonds (Beirau et al. 2012).

100 **Raman spectroscopy of titanite**

101 Several studies have applied Raman spectroscopy to titanite (Salje et al. 1993; Meyer et al. 1996;
102 Zhang and Salje 2003; Bismayer et al. 2010; Beirau et al. 2012; Zhang et al. 2013). Titanite is an
103 anisotropic phase, exhibiting Raman spectra strongly dependent on the crystallographic
104 orientation. Up to 40 different Raman bands have been reported for natural titanite samples
105 (Zhang et al. 2013), whereas other authors (Salje et al. 1993) reported only up to 30 bands.
106 Increasing degree of metamictization (Fig. 1) changes the Raman spectrum by broadening bands,

107 shifting their frequency, decreasing the overall intensity and appearance of additional bands
108 (Zhang et al. 2013). As result of metamictization, weakening of the bands at 163 cm^{-1} , 252 cm^{-1} ,
109 466 cm^{-1} , 544 cm^{-1} , 605 cm^{-1} (see Fig. 1), appearance of new bands at 574 cm^{-1} and 643 cm^{-1} ,
110 shifting of bands from 993 cm^{-1} to 978 cm^{-1} , 1017 cm^{-1} to 1008 cm^{-1} and 643 cm^{-1} to 675 cm^{-1}
111 and appearance of a shoulder at 650 cm^{-1} have been documented by (Zhang et al. 2013).

112 For estimating the degree of metamictization, Zhang et al. (2013) proposed to use the 605 cm^{-1}
113 peak as it gets broader, shifts towards 612 cm^{-1} and becomes increasingly asymmetric. Beirau et
114 al. (2012) suggested estimating the degree of metamictization from the full width at half
115 maximum (FWHM) of the 465 cm^{-1} band which arises from the SiO_4 -bending mode (Heyns et
116 al. 2000) and is narrow at low damage doses and broader at high doses. Unfortunately, both
117 approaches can be realized only at given, limited crystallographic orientation and are therefore
118 not useful as universal method for spectra taken from fragments laying in different orientations.

119 **Importance of radiation damage in (U–Th)/He thermochronology**

120 The radioactive decay of U, Th, and Sm produces α -particles (^4He nuclei). Measuring the amount
121 of both ^4He and the parent isotopes makes it possible to calculate the duration of He
122 accumulation (Farley 2002; Zeitler 2015).

123 He has a high diffusivity in solid phases, thus the preserved amount of He in a crystal depends on
124 diffusion that took place in the lifetime of the dated phase. He diffusion kinetics in crystals has
125 been intensely studied; it is controlled by temperature, mineral type, grain size (diffusion domain
126 size) and cooling rate (Zeitler et al. 1987; Wolf et al. 1996). Furthermore, mineral composition
127 and radiation damage are significant (Wolf et al. 1996; Nasdala et al. 2004; Reiners 2005).

128 Reiners and Farley (1999) have reported grain-size and cooling rate dependence of T_c in the THE
129 system at 165–225°C. However, recent studies by Baughman et al. (2017) have shown that this is
130 not valid for highly metamict grains. These authors report T_c 's of 150–210°C at low damage
131 levels and a rapid drop above a radiation damage threshold of $\sim 5 \times 10^{17} \alpha/g$ (for minimal
132 estimates of the temperature where damage accumulation starts, the threshold is $\sim 3.5 \times 10^{17} \alpha/g$).
133 Despite the lower threshold of titanite compared to zircon ($\sim 1.5 \times 10^{18} \alpha/g$; Guenther et al. 2013;
134 Baughman et al. 2017), titanite is likely to better document the higher temperature portion of a
135 protracted time-temperature path than zircon because of its usually order-of-magnitude lower
136 actinide contents (Baughman et al. 2017).

137 **Samples**

138 **Geological setting and samples from the Ilomantsi greenstone belt**

139 The samples used for this study derive from the Ilomantsi greenstone belt, which is located in
140 eastern Finland in the western part of the Neoproterozoic Karelian province (Fig. 2 and Table 1). It
141 forms part of the Ilomantsi–Kostomuksha greenstone belt, which continues into Russia and
142 extends in a N–S direction over more than 200 km. The Finnish part of this large belt (i.e.
143 Ilomantsi greenstone belt, Fig. 2) includes the ~ 50 km long Hattu schist belt, which hosts orogenic
144 gold deposits, and the Kovero belt located further southwest (Nurmi et al. 1993; Sorjonen-Ward
145 1993; Sorjonen-Ward et al. 2015). The belt is composed of dominantly felsic to intermediate
146 volcanic and siliciclastic rocks with eruption and deposition ages of 2.78–2.75 Ga (Vaasjoki et al.
147 1993; Huhma et al. 2012b) and small elongated plutons with emplacement ages of ~ 2.75 – 2.70 Ga
148 (Vaasjoki et al. 1993; Käpyaho et al. 2016).

149 The Ilimantsi greenstone belt was affected by two metamorphic events. The Neoproterozoic
150 metamorphism reached amphibolite facies peak conditions ($550\pm 50^\circ\text{C}$, 3–5 kbar; O'Brien et al.
151 1993). An ~ 2.70 Ga minimum (e.g. cooling) age for this metamorphism was deduced from 2.708
152 and 2.696 Ga U–Pb ages of titanite and monazite from granodiorite and leucogranite intrusions,
153 respectively (Vaasjoki et al. 1993). However, Hölttä et al. (2016) proposed 2.66 Ga and 2.62 Ga
154 age for the Neoproterozoic metamorphism based on dating of monazite growth. During the Lapland–
155 Savo orogenic phase of the Paleoproterozoic Svecofennian orogeny, thick, east–verging nappes
156 were emplaced on the Archean basement of eastern Finland and temperatures in the Ilimantsi
157 greenstone belt reached $400\text{--}500^\circ\text{C}$ as indicated by partial reset of hornblende K–Ar ages
158 (Kontinen et al. 1992) and Pb isotope exchange studies (Halla and Heilimo 2009). Biotite K–Ar,
159 as well as biotite and muscovite Ar–Ar ages suggest cooling below $\sim 350\text{--}300^\circ\text{C}$ at ~ 1.8 Ga
160 (Kontinen et al. 1992; Molnár et al. 2016).

161 The later orogenies and accretionary events that occurred in Fennoscandia, such as the Gothian
162 (1.64–1.52 Ga) and the Telemarkian accretion (1.52–1.48 Ga), the Hallandian and Danopolonian
163 orogenies (1.47–1.42 Ga) and the Sveconorwegian orogeny (1.14–0.90 Ga) (Bingen et al. 2008)
164 affected mainly the southwestern margin of Fennoscandia and were of little and poorly
165 understood impact for eastern Finland. The lack of sedimentary record makes the reconstruction
166 of the post–Svecofennian thermal evolution difficult (Kohonen 2005).

167 A kaoline deposit at Virtasalmi, ~ 200 km WSW of the Ilimantsi greenstone belt, indicates
168 surface exposure of the Svecofennian crystalline basement during the Mesoproterozoic at ~ 1.18
169 Ga (Sarapää 1996). Late Neoproterozoic, in Fennoscandia referred to as Vendian, and Cambrian
170 sediments are common further south in Estonia. The extent of this unconformity and sediment

171 coverage towards north (e.g. Finland) is not clear and has been a matter of discussion (Puura et
172 al. 1996; Larson et al. 1999; Sliupa et al. 2006).

173 Thermochronologic data from eastern Finland comprise of a wide range of Neoproterozoic and
174 early Paleozoic apatite fission track (AFT) and apatite (U–Th)/He (AHe) ages (Lehtovaara 1976;
175 Lorencak 2003; Murrell 2003; Murrell and Andriessen 2004; Kohn et al. 2009). In combination
176 with new ZHe, THe and AHe data (Heller et al. in preparation) they indicate that the Ilomantsi
177 greenstone belt experienced slow cooling since the Svecofennian orogeny and that temperatures
178 did not exceed 100°C for the last 1.0 Ga.

179 For calculation of radiation damage densities the duration of α -damage accumulation has to be
180 estimated. However, neither the thermal history of the samples in the time interval of 1.8-1.5 Ga
181 (see below), nor the temperature range of α -damage annealing are well defined. While it is a
182 common praxis to estimate that annealing of α -damage occurs at similar temperatures as
183 annealing of fission tracks (Baughman et al. 2017 for titanite and Pidgeon 2014 for zircon),
184 experiments by Gleadow (1978) indicate that α -damage annealing of titanites occurs mainly in
185 the lower part of the titanite fission track partial annealing zone (TPAZ). For the TPAZ different
186 estimates exist (197°C: Naeser and Forbes 1976; 260±20°C Gleadow and Lovering 1978; 250 ±
187 50°C: Gleadow and Brooks 1979; 240 ± 40°C: Harrison et al. 1979; 275 ± 25°C: Fitzgerald and
188 Gleadow 1988; 275 ± 25°C: Kohn et al. 1993; 265–310°C: Coyle and Wagner 1998). Studies
189 including thermal annealing experiments (Bismayer et al. 2010; Beirau et al. 2012; Salje et al.
190 2012) indicate that α -damage annealing is a complex process occurring over a temperature range;
191 while recovery of point defect is possible at lower temperatures ($T < 300^\circ\text{C}$), relevant
192 recrystallization of amorphous areas happens only at $T > 320^\circ\text{C}$. However, note that temperature

193 estimates from thermal annealing experiments are often too high as they don't include geological
194 timescales.

195 In our case the onset of α -damage accumulation can be bracketed to 1.5–1.8 Ga. The upper limit
196 is given by the ~1.8 Ga biotite and muscovite K–Ar and Ar–Ar ages (Kontinen et al. 1992;
197 Molnár et al. 2016). Note that Kohn et al. (1993) report that K–Ar ages are always greater or
198 equal to titanite fission track ages. The lower bracket is given by the oldest THE Ages (~1.5 Ga)
199 of our samples, which in our case of typical grains sizes and slow cooling correspond to
200 temperatures of ~180°C.

201 The time interval from 1.5–1.8 Ga thus corresponds to a temperature drop from ~300°C to
202 ~180°C, the onset of α -damage accumulation lies somewhere in between. Assuming that post-
203 metamorphic cooling was faster in the beginning and then slowed down we decided to calculate
204 with 1.7 Gy as damage accumulation duration. However, due to the uncertainties involved, we
205 also present the results for 1.8, 1.6 and 1.5 Gy accumulation duration and discuss the respective
206 error below.

207 The sample set with relatively high damage densities from the Ilomantsi belt was complemented
208 by some well-studied titanites (partly reference materials for U-Pb geochronology) of
209 considerably lower α -doses (Table 2).

210 **Methods**

211 **Sample preparation**

212 The mineral separation has been performed at the Geological Survey of Finland. The samples
213 were crushed, sieved and titanite fractions were separated by density and magnetic methods. For

214 single grain analysis, inclusion-free titanite fragments from the 63–200 μm sieve fractions were
215 handpicked. 2 to 5 aliquots of 19 different samples from Finland were chosen. For the polished
216 mineral grain mounts 9 Finnish samples as well as 6 low-damage samples were mounted in
217 epoxy resin discs, ground and diamond-polished.

218 **Raman spectroscopy**

219 Raman measurements were done on (i) unmounted crystal fragments and (ii) polished grain
220 mounts. The measurements were performed with a Horiba XPlora Plus system equipped with a
221 532 nm excitation laser (25 mW maximum output power) and an Olympus BX41 microscope,
222 which is coupled to a 200 mm focal length spectrograph with a four-grating turret. The system
223 has a Multi-Pinned-Phase (MPP) open-electrode CCD detector with a precision of ± 1 pixel.
224 Using 532nm the spectral resolution is 1.4 cm^{-1} with the 2400 grooves/mm grating and 2.5 cm^{-1}
225 with the 1800 grooves/mm grating. For the unmounted crystal fragments, the 1800 grooves/mm
226 grating was used and the Raman spectra were collected for 2×10 seconds at 50% laser power
227 with 20x (0.4 NA) or 50x LWD (0.5 NA) objective in 1–3 spots per crystal fragment. The grain
228 mounts were measured with the 2400 grooves/mm grating at 10% laser power with 50x LWD
229 objective. Measurement times were 3×5 to 3×20 seconds depending on signal strength.

230 The positional drift of the spectrometer was checked regularly by measurement of a Si standard
231 and is negligible for this dataset. In transparent crystals the penetration depth is about $\sim 15\text{ }\mu\text{m}$ for
232 the 50x LWD objective and $\sim 20\text{ }\mu\text{m}$ for the 20x objective. The theoretical diameter of the Raman
233 spots are $\sim 1.3\text{ }\mu\text{m}$ (50x LWD) and $\sim 1.6\text{ }\mu\text{m}$ (20x).

234 Spectra were recorded in the range $100\text{--}1800\text{ cm}^{-1}$. For detection of possible photoluminescence
235 bands additional Raman spectra were taken on some selected grains with a Horiba Jobin-Yvon

236 Labram HR800UV spectrometer equipped with a 633 nm excitation laser. Titanite spectra with a
237 superposed epoxy signal were not used for further evaluation.

238 **Curve-fitting of the Raman spectra**

239 The curve-fitting and spectral evaluation were performed with the IFORS software (Lünsdorf
240 and Lünsdorf 2016). The signal part of the spectrum was modeled by pseudo-Voigt functions
241 (pV-functions). In each iteration, a new function was added to the model, and the sum of the
242 squared residuals was reduced by randomly changing a function parameter (e.g. center position,
243 height, width, or shape-factor) by a random value. Two main approaches were applied: (i) using
244 IFORS for background correction and curve-fitting, and (ii) manual background correction using
245 the Fityk software (Wojdyr 2010) followed by automated curve-fitting with IFORS.

246 Reasonable fitting parameters were found by testing different evaluation constraints and visually
247 checking the quality of the fit. The tested parameter values as well as the best configuration setup
248 can be found in Table 3 and Appendix 1.

249 During the curve-fitting, the spectrum is first scaled to 100 arbitrary intensity units and, in case
250 of automated background correction, the estimated baseline is subtracted in a second step. Thus,
251 the comparison of integrated intensities (by summing the areas of all pV-functions) and function
252 areas is only possible in evaluations without automated background correction.

253 The fitted band widths (FWHM = full width at half maximum) of the titanite spectra were
254 corrected for the apparatus function after Irmer (1985) and Nasdala et al. (2001).

255 **Determination of the concentration of α -emitting elements and the (U-Th)/He ages**

256 **Unmounted titanite crystal fragments**

257 For U and Th concentration measurements and (U–Th)/He age determination clear, inclusion–
258 free fragments without external crystal surfaces were hand-picked using a stereo- and a
259 polarizing microscopes. These fragments were photographed and wrapped in platinum capsules
260 with 1x1 mm size. The analysis involved three separate steps: 1) He extraction and measurement
261 2) chemical digestion and 3) measurement of the parent isotopes.

262 For the He measurement the crystals were degassed in a high vacuum extraction line using an
263 infrared laser. A Ti–Zr getter at 450°C was used to purify the gas. The inert gases were measured
264 by a Hiden triple–filter quadrupole mass spectrometer with a positive ion–counting detector. For
265 every sample a re–extraction was done to check the complete degassing of the crystal fragment.

266 For determination of the mass of U, Th and Sm the degassed titanite fragments were dissolved in
267 a mixture of concentrated ultrapure HCl (500 µl) and HF (100 µl) (Reiners and Farley 1999) in
268 pressurized teflon vials during one day at 220°C, and spiked with calibrated ²³⁰Th and ²³³U
269 solutions. After cooling, the samples were dried, converted to nitrate by re–dissolving in 0.25–
270 1 ml 65% HNO₃ and after a further drying step dissolved in a mixture of 4% HNO₃ with 0.05%
271 HF.

272 U, Th, Sm and other REE measurements were performed using a Perkin Elmer Elan DRC II
273 assembled with an APEX MicroFlow nebulizer and a Thermo iCAP Q ICP–MS instrument. The
274 actinides were determined by isotope dilution technique, while for Ca, Ti and the other trace
275 elements the external calibration method was applied.

276 **Mounted titanite fragments**

277 The trace element content of titanite grains mounted in polished epoxy resin discs was analyzed
278 by Laser–Ablation ICP–MS. A Resonetics excimer laser was used, coupled to a Thermo

279 Element 2 sector field mass spectrometer. Measurements were conducted at the same spots as the
280 Raman measurements and performed with 10 μm laser beam diameter and short ablation times.
281 For conversion of the cps data to concentrations the NIST610 and TNT1500 glass standards were
282 used (Klemme et al. 2008).

283 **Results**

284 **Raman spectra**

285 82 Raman spectra of 63 unmounted crystal fragments from 19 Finnish samples were acquired, as
286 well as 152 spectra of 9 titanite mounts of the Finnish samples and 59 spectra of 6 mounted low-
287 damage samples, totaling 293 titanite Raman spectra.

288 The Raman spectra show a broad variation in band widths, absolute and relative intensities of the
289 bands, as well as shifts in band positions. Figure 1 shows two very different spectra obtained on
290 grains with different α -doses. At the acquisition of the spectra the crystals were randomly
291 oriented, thus the entire range of anisotropy effects is represented (see e.g. Beirau et al. 2012;
292 Zhang et al. 2013).

293 Due to the edge-filter, which blocks the signal below $\sim 70\text{ cm}^{-1}$, most spectra start with signal and
294 many have high Raman intensities at $100\text{--}200\text{ cm}^{-1}$. Therefore, the background signal is
295 detectable only at higher wavenumbers ($>1000\text{ cm}^{-1}$, Figure 1).

296 For an excitation wavelength of 532 nm the major photoluminescence bands (Sm, Nd) occur at
297 higher wavenumbers than the titanite Raman bands (Lenz et al. 2015). The comparison of the
298 spectra with spectra acquired with 633 nm excitation shows no differences, which indicates that
299 no REE-related photoluminescence signals overlie the Raman signal. The only

300 photoluminescence that theoretically occurs in the Raman wavenumber range is an Er-generated
301 peak at 564 nm (i.e. =1060 cm⁻¹), but this has not been detected.

302 **Effective uranium (eU) contents and α -doses**

303 The eU contents of the studied titanite crystal fragments range from 6 ppm to 935 ppm. The α -
304 doses were calculated as:

$$D_{\alpha} = 8 \cdot \frac{C_U \cdot N_A \cdot 0.9928}{M_{238} \cdot 10^6} \cdot (exp^{\lambda_{238} \cdot t} - 1) \\ + 7 \cdot \frac{C_U \cdot N_A \cdot 0.0072}{M_{235} \cdot 10^6} \cdot (exp^{\lambda_{235} \cdot t} - 1) \\ + 6 \cdot \frac{C_{Th} \cdot N_A}{M_{232} \cdot 10^6} \cdot (exp^{\lambda_{232} \cdot t} - 1)$$

305 (Eq. 1)

306 where C = actinide concentrations (in ppm), N_A = Avogadro's number (6.022×10^{23} atoms/mol),
307 M = the molecular masses, λ = the decay constants for the different isotopes, and t = the onset of
308 damage accumulation (t is 1.7 Ga for the Finnish samples as discussed above or the respective
309 ages of the low damage titanites, see Table 2). The α -doses of the Finnish samples range from
310 4×10^{16} to 2.9×10^{18} α /g and those of the additional samples with lower α -dose from 1.3×10^{13}
311 to 1.8×10^{17} α /g (Appendix 2). Altogether, the α -dose in the samples ranges over more than five
312 orders of magnitude.

313 **Quality of the curve-fitting of the Raman spectra**

314 In order to establish reasonable curve-fitting parameters and comparison of their effects on
315 further calculations, we applied a systematic sensitivity study and several curve-fitting protocols

316 were tested (Table 3 and Appendix 1). For the completely automated fittings (including
317 automated background correction), reasonable results (setting “wf_sm”) were achieved when
318 using a “*window_filter*” parameter with 0.35 window size for baseline calculation, setting the
319 “*noise*” parameter to 2.5 or 3, allowing 40 pV–functions and smoothing the spectra with a
320 “*smoothing size*” parameter of 9 (for all other parameter see Appendix 1). Lower “*noise*”
321 parameter values lead to a solution with many small pV–functions while higher “*noise*”
322 parameter values or severe restrictions on the maximum number of allowed pV–functions either
323 lead to incomplete curve–fits (i.e. some bands were not described by pV–function) or imprecise
324 fitting of broad bands. In most cases, three repeated curve–fits yielded consistent, well
325 reproducible results. Only a very minor proportion of the spectra showed poor reproducibility.

326 A problem during curve–fitting of metamict titanite spectra is the inherently unknown
327 background at low wavenumbers. Assuming a flat baseline, even at low wavenumbers seems to
328 be reasonable, however, dispersed light at low wavenumbers might cause some increase in the
329 background intensity. This is why we tested both the automated and the manual background
330 correction. The automated curve–fitting often estimates a baseline which is elevated at low
331 wavenumbers (Fig. 1). Too small “*window size*” parameter values (e.g. 0.25) produced
332 unreliable, bended baselines. For manual background correction a flat baseline (i.e. not elevated
333 at lower wavenumbers) was assumed.

334 The curve–fitting sometimes produces unapparent solutions; the most common type is when a
335 range in the spectrum is modeled by fitting of one flat, wide pV–function and three small narrow
336 pV–functions instead of a triplet with three medium sized functions. The only way to avoid the
337 dubious flat wide pV–functions is by limiting the “*maximum peak width*” parameter. Setting the
338 “*maximum peak width*” parameter to 80 or 100 cm^{-1} (given as HWHM = half width at half

339 maximum) caused fewer artifacts than allowing it to become as high as 150 cm^{-1} . However, harsh
340 restriction of the pV–function width (e.g. values below 80 cm^{-1}) is critical because in our case the
341 widths are the most important result of the curve–fitting procedure.

342 **Possibilities of α –dose estimation from the Raman spectra**

343 **Single band testing**

344 Beirau et al. (2012) proposed the use of the FWHM of the 465 cm^{-1} band, which is assigned to
345 the SiO_4 –bending mode (Heyns et al. 2000; Heyns and Harden 2013), as an estimator for the
346 degree of metamictization because it broadens with increasing α –dose. Figures 3A and 3B show
347 the FWHM of this band (defined by the center values between 458 cm^{-1} and 468 cm^{-1}) versus the
348 α –dose of each spot (Appendix 3). The colors of the data points indicate the band position. In
349 very low damage samples, the band has a width of $\sim 20 \text{ cm}^{-1}$ and centers at $\sim 468 \text{ cm}^{-1}$. Above
350 $\sim 5 \times 10^{16} \alpha/\text{g}$ the band starts getting broader and shifts towards lower wavenumbers. However, for
351 highly damaged crystals the band widths are very scattered (Fig. 3A) and an accurate estimation
352 becomes difficult. Another problem with the use of this band is its absence in some spectra.

353 The band at 424 cm^{-1} (415 cm^{-1} to 425 cm^{-1} , Figs. 3C and 3D), which is also assigned to the SiO_4 –
354 bending mode (Heyns et al. 2000; Heyns and Harden 2013), shows a very similar behavior. Both
355 width and position correlate with the α –dose (Appendix 4). Starting from $\sim 5 \times 10^{16} \alpha/\text{g}$, band
356 broadening from $\sim 18 \text{ cm}^{-1}$ to $>50 \text{ cm}^{-1}$ and positional shift from 424 cm^{-1} to 416 cm^{-1} are
357 observed. The 424 cm^{-1} band also does not appear in all spectra.

358 The bands at 163 cm^{-1} , 252 cm^{-1} , 544 cm^{-1} and 605 cm^{-1} for which Zhang et al. (2013) report
359 band broadening, as well as the band at 535 cm^{-1} were likewise investigated. However, we could
360 not determine significant correlations. For the bands at 163 cm^{-1} , 252 cm^{-1} and 535 cm^{-1} the band

361 widths are scattered and show poor positive correlation with the α -dose while the positions
362 appear to be uncorrelated. For the band at 544 cm^{-1} neither the width nor the position shows any
363 correlation with the α -dose.

364 According to Zhang et al. (2013) the band at 605 cm^{-1} broadens, shifts towards 612 cm^{-1} and
365 becomes more asymmetric with increasing metamictization. However, Beirau et al. (2012) show,
366 that depending on the orientation the band either shifts towards higher wavenumbers or shifts
367 towards lower wavenumbers. Verifying this behavior is hindered by the asymmetric character of
368 the band. Most of the curve-fits contain at least one pV-function in the range of $590\text{--}620\text{ cm}^{-1}$,
369 some contain 2, rarely 3 pV-functions could be fitted. No correlations with α -dose were
370 observed.

371 **Characterization of the entire Raman spectrum**

372 Metamictization influences some bands more than others but generally it broadens all Raman
373 bands (Zhang et al. 2013). In order to relate this general broadening with the corresponding α -
374 doses we looked for parameters which describe the modification of the spectra with a single
375 value. We calculated medians, unweighted and weighted means of all band widths for every
376 spectrum. The use of the mean pV-function areas was also considered in some test calculations,
377 however, it turns out that the comparison of the function areas is biased in all spectra using
378 automated background correction, because the absolute areas are affected by the baseline height.
379 The use of mean width values instead of single band widths has distinct advantages in the case of
380 metamict titanite where the fitting is hampered by overlapping and asymmetric bands.

381 For the loose grains where two or three spectra were recorded, means and medians combining the
382 two or three spectra were calculated. FWHM means were weighted either by (i) scaled pV-

383 function intensity (iw-FWHM) or by (ii) scaled pV-function area (aw-FWHM). To test the
384 reproducibility all spectra were curve-fitted three times. Means and medians were calculated for
385 each curve-fit as well as for the average spectrum joining all three evaluations. Usually, the
386 numeric difference between the three repetitions is less than 10%, but can be as high as 20% for
387 some spectra (due to overlapping broad bands). Therefore, the use of repeated spectral
388 evaluations and means over all evaluations is highly recommended. The (weighted) means and
389 medians were compared for all tested curve-fitting protocols. All data can be found in Appendix
390 2.

391 All means and medians show good correlation with the α -dose (nearly all p-values $\ll 2.2 \times 10^{-16}$).
392 However, unweighted means and medians are much more sensitive to the curve-fitting
393 parameters and spectral properties (e.g. signal-to-noise ratio) than weighted means. Examples
394 are presented in Appendix 5.

395 The use of weighted mean FWHM has the advantage that it is less sensitive to the total number
396 of used pV-functions and the larger pV-functions have stronger influence than small peaks.
397 Moreover, the weighted mean FWHMs, especially iw-FWHMs, are much more robust because
398 different curve-fitting protocols yield nearly the same results (see Fig. 4). The iw-FWHM yield a
399 better result than the aw-FWHM. The dependency of some bands on the orientation of the crystal
400 seems to have only minor impact on the iw-FWHM.

401 **The most important sensitivity test: influence of the maximum number of pV-functions on** 402 **the curve-fitting results**

403 We demonstrated that the iw-FWHM procedure leads to more consistent results than the area-
404 weighted procedure. Thus, a systematic sensitivity test series was performed to study the impact

405 of the maximum number of pV-functions on the results of the curve-fitting. The repeated
406 evaluations allowed for 10, 15, 20, 30 or 40 pV-functions. Allowing 15 up to 40 pV-functions
407 we recorded always the same trend (see Figs. 4 and 5). However, with only 10 pV-functions the
408 spectra were often poorly fitted and especially in the well-crystalline samples not all bands were
409 described by pV-functions resulting in higher iw-FWHM values. Thus, curve-fitting with a
410 maximum of 15 pV-functions is sufficient to characterize the α -dose in titanites by the iw-
411 FWHM method, even if these 15 pV-functions might not represent the spectra in all details.

412 **Discussion**

413 Our results suggest that the intensity weighted mean FWHM is a reliable parameter to describe
414 the α -dose in titanite. The restriction to maximal 15 pV-functions led to consistent results.
415 Below an α -dose of 5×10^{16} α/g the iw-FWHM is independent of α -dose and scatters between
416 25 cm^{-1} and 50 cm^{-1} . Above this value, the iw-FWHM increases linearly with increasing α -dose
417 up to $3 \times 10^{18} \alpha/g$.

418 Figure 5A compares the linear regression parameters (slope, y-axis intercept and R^2) of all
419 calculated values for all tested curve-fitting protocols. All linear regression data can be found in
420 Appendix 6. The iw-FWHM linear regressions yield the tightest cluster of results associated with
421 high coefficients of determination (Fig. 5A). All the other methods yield more scattered results
422 and especially the median linear regressions have often very low coefficients of determination.
423 This implies that regardless of the curve-fitting protocol used for spectral evaluation, the iw-
424 FWHM method produced nearly the same linear regression, which makes this method the most
425 robust of all tested procedures.

426 Thus, we recommend to use the iw-FWHM as radiation damage estimator for titanite. For the
427 highest density point in Figure 5A the formula for the linear increase of the iw-FWHM with
428 growing α -dose is $\text{iw-FWHM}[\text{cm}^{-1}] \sim 39.2[\text{cm}^{-1}] + 3.82 \times 10^{-17}[\text{cm}^{-1}/(\alpha/\text{g})] \times \alpha\text{-dose}[\alpha/\text{g}]$. This is
429 similar to the formula for the most satisfying protocol “wf_sm” (see details in Appendix 1),
430 which is $\text{iw-FWHM}[\text{cm}^{-1}] \sim 38.8(\pm 1.2)[\text{cm}^{-1}] + 3.86(\pm 0.13) \times 10^{-17}[\text{cm}^{-1}/(\alpha/\text{g})] \times \alpha\text{-dose}[\alpha/\text{g}]$.
431 Combining both formulae we get $\text{iw-FWHM}[\text{cm}^{-1}] \sim 39.0(\pm 1.2)[\text{cm}^{-1}] + 3.84(\pm 0.13) \times 10^{-17}[\text{cm}^{-1}/(\alpha/\text{g})] \times \alpha\text{-dose}[\alpha/\text{g}]$. The constants of the regression equation are determined by ca. 3% relative
432 uncertainties.
433

434 The other, even more important bias that controls the accuracy of the constants comes from the
435 assumed duration of the damage accumulation. As discussed above, the temperature range where
436 radiation damage accumulation starts for the Finnish samples is not known precisely, neither is
437 the annealing behavior in titanite. It is not clear how the density of accumulated damage
438 influences the annealing kinetics, and the effect of the variable chemical composition of titanite is
439 not known. Additionally the thermal history of the Finnish samples bears some uncertainty in the
440 interval of 1.8–1.5 Ga. Figure 5B visualizes the effect of this uncertainty on the linear
441 regressions. While the y-intercepts remain unchanged, shorter damage accumulation durations
442 lead to steeper slopes as the absolute damage gets smaller. This uncertainty is higher than the
443 error derived from the spread of the data. Including this uncertainty into the error of the linear
444 regression leads to a corrected calibration line: $\text{iw-FWHM}[\text{cm}^{-1}] \sim 39.0(\pm 1.2)[\text{cm}^{-1}] + 3.84(+0.61, -$
445 $0.26) \times 10^{-17}[\text{cm}^{-1}/(\alpha/\text{g})] \times \alpha\text{-dose}[\alpha/\text{g}]$.

446 The onset of the significant change of the titanite Raman peak width is around $5 \times 10^{16} \alpha/\text{g}$.
447 Baughman et al. (2017) studied the He diffusivity and the THe closure temperature in relation to
448 the α -dose. Their data indicate a threshold, where T_c strongly decreases at around $\sim 5 \times 10^{17} \alpha/\text{g}$

449 (Fig. 4). It is remarkable that our procedure based on the characterization of the entire Raman
450 spectrum is more sensitive and detects the change of the lattice at one order of magnitude lower
451 level. This indicates the need of further He diffusion experiments in order to quantify the
452 diffusion parameters for titanite in the relatively low damage range.

453 **Comparison with (U-Th)/He results**

454 For some of the Finnish samples (U-Th)/He ages were determined. Figure 6A shows these ages
455 compared to their α -dose and eU content. The data show a negative correlation and the covered
456 eU range is relatively small. Compared to our data, the data presented by Baughman et al. (2017)
457 shows a better negative correlation and includes higher eU contents.

458 Figure 6B shows the THe age versus the iw-FWHM (fitting with 15 pV-functions). As expected,
459 the data show a negative correlation, however, the spread is high. Possible reasons for the
460 dispersion include the moderate correlation of THe age and α -dose, especially at low α -doses,
461 influence of REE on THe ages, alpha ejection correction (Farley et al. 1996; Stockli and Farley
462 2004), zoning and inclusions (the details are discussed in Heller et al. in prep).

463 Estimation of the α -dose cannot substitute the THe age determination, however, it enables a pre-
464 selection of the grains most appropriate for the target of a specific study.

465 **Implications**

466 We present a robust Raman spectroscopy based method for estimating the α -dose in titanite by
467 Raman spectroscopy. The titanite (U-Th)/He thermochronometer is relevant for the
468 reconstruction of thermal histories in the upper crust, because titanite occurs in more mafic
469 lithologies, in contrast to zircon, and its typically lower actinide content allows for obtaining

470 reliable thermochronologic information in cratonic areas that experienced cooling in Precambrian
471 times. The method can be used in two ways for the routine work in (U–Th)/He
472 thermochronology: (i) It can provide an easy-to-apply and quick tool for identifying highly
473 damaged titanite grains that have extremely low closure temperature due to the high α -dose. In
474 such crystals the recoil and fission tracks are already in contact and provide a kind of
475 "percolation" leading to very quick helium diffusion (Baughman et al. 2017). Rejecting these
476 titanite grains can optimize the dating procedure by analyzing only the better crystalline grains
477 for which the closure temperature is considerable above the ambient temperature. (ii) The other
478 approach is to concentrate on the wide range of the α -doses and aim at involving grains that
479 represent both extremely low and high α -doses in order to perform a batch modelling (e.g. Orme
480 et al. 2016; Johnson et al. 2017; Hueck et al. 2018). In this way the thermal history may be
481 described with better confidence and even the lower temperature ranges may be better
482 constrained by the titanite grains with very low closure temperature. The method proposed here
483 provides a pre-selection method in order to optimize the range of α -doses of the dated grains.

484 **Acknowledgement**

485 We would like to thank Hannu Huhma and the Geological Survey of Finland (GTK) for
486 providing of the sample material.

487 **References**

488 Ault, A.K., Guenther, W.R., Moser, A.C., Miller, G.H. and Refsnider, K.A. (2018) Zircon grain
489 selection reveals (de)coupled metamictization, radiation damage, and He diffusivity. *Chemical*
490 *Geology*, 490, 1–12.

- 491 Baughman, J.S., Flowers, R.M., Metcalf, J.R. and Dhansay, T. (2017) Influence of radiation
492 damage on titanite He diffusion kinetics. *Geochimica et Cosmochimica Acta*, 205, 50–64.
- 493 Beirau, T., Bismayer, U., Mihailova, B., Paulmann, C. and Groat, L.A. (2010) Structural
494 phenomena of metamict titanite : a synchrotron , X-ray diffraction and vibrational spectroscopic
495 study. *Phase Transitions*, 83, 694–702.
- 496 Beirau, T., Mihailova, B., Malcherek, T., Paulmann, C., Bismayer, U. and Groat, L.A. (2014)
497 Temperatur-induced P21/c to C2/c phase transition in partially amorphous (metamict) titanite
498 revealed by Raman Spectroscopy. *The Canadian Mineralogist*, 52, 91–100.
- 499 Beirau, T., Mihailova, B., Matveeva, G., Kolb, U., Malcherek, T., Groat, L.A. and Bismayer, U.
500 (2012) Structural anisotropy and annealing-induced nanoscale atomic rearrangements in
501 metamict titanite. *American Mineralogist*, 97, 1354–1365.
- 502 Beirau, T., Nix, W.D., Ewing, R.C., Schneider, G.A., Groat, L.A. and Bismayer, U.
503 (2016) Mechanical properties of natural radiation-damaged titanite and temperatureinduced
504 structural reorganization: A nanoindentation and Raman spectroscopic study. *American*
505 *Mineralogist*, 101, 399–406.
- 506 Bingen, B., Andersson, J., Söderlund, U. and Möller, C. (2008) The Mesoproterozoic in the Nordic
507 countries. *Episodes*, 31, 29–34.
- 508 Bismayer, U., Paulmann, C., Groat, L. and Zhang, M. (2010) Local phenomena in metamict
509 titanite. *Acta Physica Polonica A*, 117, 74–77.
- 510 Butler, R.F., Gehrels, G.E., Baldwin, S.L. and Davidson, C. (2002) Paleomagnetism and
511 geochronology of the Ecstall pluton in the Coast Mountains of British Columbia: Evidence for
512 local deformation rather than large-scale transport. *Journal of Geophysical Research*, 107.

- 513 Cherniak, D.J. and Watson, E.B. (2011) Helium diffusion in rutile and titanite, and consideration
514 of the origin and implications of diffusional anisotropy. *Chemical Geology*, 288, 149–161.
- 515 Coyle, D.A. and Wagner, G.A. (1998) Positioning the titanite fission-track partial annealing
516 zone. *Chemical Geology*, 149, 117–125.
- 517 Farges, F. (1997) Fivefold-coordinated Ti⁴⁺ in metamict zirconolite and titanite: A new
518 occurrence shown by Ti K-edge XANES spectroscopy. *American Mineralogist*, 82, 44–50.
- 519 Farley, K.A. (2002) (U-Th)/He Dating: Techniques, Calibrations, and Applications. *Reviews in*
520 *Mineralogy and Geochemistry*, 47, 819–844.
- 521 Farley, K.A., Wolf, R.A. and Silver, L.T. (1996) The effects of long alpha-stopping distances on
522 (U-Th)/He ages. *Geochimica et Cosmochimica Acta*, 60, 4223–4229.
- 523 Fitzgerald, P.G. and Gleadow, A.J.W. (1988) Fission-track geochronology, tectonics and
524 structure of the Transantarctic Mountains in northern Victoria Land, Antarctica. *Chemical*
525 *Geology*, 73, 1497–1502.
- 526 Flowers, R.M. (2009) Exploiting radiation damage control on apatite (U-Th)/He dates in cratonic
527 regions. *Earth and Planetary Science Letters*, 277, 148–155.
- 528 Flowers, R.M., Ketcham, R.A., Shuster, D.L. and Farley, K.A. (2009) Apatite (U-Th)/He
529 thermochronometry using a radiation damage accumulation and annealing model. *Geochimica et*
530 *Cosmochimica Acta*, 73, 2347–2365.
- 531 Gaal, G. (1980) Geological setting and intrusion tectonics of the Kotalahti nickelcopper deposit,
532 Finland. *Bulletin of the Geological Society of Finland*, 52, 101–128.
- 533 Gautheron, C., Tassan-Got, L., Barbarand, J. and Pagel, M. (2009) Effect of alpha-damage
534 annealing on apatite (U-Th)/He thermochronology. *Chemical Geology*, 266, 166–179.

- 535 Gleadow, A.J.W. (1978) Anisotropic and variable track etching characteristics in natural sphenes.
536 Nuclear Track Detection, 2, 105–117.
- 537 Gleadow, A.J.W. and Brooks, C. (1979) Fission-track dating, thermal histories and tectonics of
538 igneous intrusions in east Greenland. Contributions to Mineralogy and Petrology, 71, 45–60.
- 539 Gleadow, A.J.W. and Lovering, J.F. (1978) Thermal history of granitic rocks from western
540 Victoria: A fission-track dating study. Journal of the Geological Society of Australia, 25, 323–
541 340.
- 542 Groat, L.A., Carter, R.T., Hawthorne, F.C. and Ercit, T.S. (1985) Tantalian niobian titanite from
543 the Irgon claim, southeastern Manitoba. Canadian Mineralogist, 23, 569–571.
- 544 Guenther, W.R., Reiners, P.W., Drake, H. and Tillberg, M. (2017) Zircon, titanite, and apatite
545 (U-Th)/He ages and age-eU correlations from the Fennoscandian Shield, southern Sweden.
546 Tectonics, 36, 1254–1274.
- 547 Guenther, W.R., Reiners, P.W., Ketcham, R.A., Nasdala, L. and Giester, G. (2013) Helium
548 diffusion in natural zircon: radiation damage, anisotropy, and the interpretation of zircon (U-
549 TH)/He thermochronology. American Journal of Science, 313, 145–198.
- 550 Halla, J. (2002) Origin and Paleoproterozoic reactivation of Neoproterozoic high-K granitoid rocks
551 in eastern Finland. Annales Academiae Scientiarum Fennicae, Geologica - Geographica, 163.
- 552 Halla, J. and Heilimo, E. (2009) Deformation-induced Pb isotope exchange between K-feldspar
553 and whole rock in Neoproterozoic granitoids: Implications for assessing Proterozoic imprints.
554 Chemical Geology, 265, 303–312.
- 555 Harangi, S., Lukács, R., Schmitt, A.K., Dunkl, I., Molnár, K., Kiss, B., Seghedi, I., Novothny and
556 Molnár, M. (2015) Constraints on the timing of Quaternary volcanism and duration of magma

- 557 residence at Ciomadul volcano, east-central Europe, from combined U-Th/He and U-Th zircon
558 geochronology. *Journal of Volcanology and Geothermal Research*, 301, 66–80.
- 559 Harrison, T.M., Armstrong, R.L., Naeser, C.W. and Harakal, J.E. (1979) Geochronology and
560 thermal history of the Coastal Plutonic Complex, near Prince Rupert, British Columbia. *Canadian*
561 *Journal of Earth Sciences*, 16, 400–410. Hawthorne, F.C., Groat, L.A., Raudsepp, M., Ball, N.A.,
562 Kimata, M., et al. (1991) Alpha-decay damage in titanite. *American Mineralogist*, 76, 370–396.
- 563 Heilimo, E., Halla, J. and Huhma, H. (2011) Single-grain zircon U-Pb age constraints of the
564 western and eastern sanukitoid zones in the Finnish part of the Karelian Province. *Lithos*, 121,
565 87–99.
- 566 Heyns, A.M. and Harden, P.M. (2013) The temperature dependence of the Raman spectra of
567 chromium-doped titanite (CaTiOSiO₄). *Journal of Raman Spectroscopy*, 44, 1615–1624.
- 568 Heyns, A.M., Harden, P.M. and Prinsloo, L.C. (2000) Resonance Raman study of the high-
569 pressure phase transition in chromium-doped titanite, CaTiOSiO₄. *Journal of Raman*
570 *Spectroscopy*, 31, 837–841.
- 571 Higgins, J.B. and Ribbe, P.H. (1976) Crystal-chemistry and space groups of natural and synthetic
572 titanites. *American Mineralogist*, 61, 878–888.
- 573 Hölttä, P., Lehtonen, E., Lahaye, Y. and Sorjonen-Ward, P. (2016) Metamorphic evolution of the
574 Ilomantsi greenstone belt in the Archaean Karelia Province, eastern Finland. In J. Halla, M.J.
575 Whitehouse, T. Ahmad and Z. Bagai, Eds., *Crust-Mantle Interactions and Granitoid*
576 *Diversification: Insights from Archean Cratons*. Vol. 449. Special Publications. Geological
577 Society London, London.

- 578 Heberer, B., Reverman R.L., Fellin, M.G., Neubauer, F., Dunkl, I., Zattin, M., Seward, D.,
579 Genser, J. and Brack, P. (2017) Postcollisional cooling history of the Eastern and Southern Alps
580 and its linkage to Adria indentation. *International Journal of Earth Sciences*, 106, 1557–1580.
- 581 Hueck, M., Dunkl, I., Heller, B., Basei, M.A.S. and Siegesmund, S. (2018) (U-Th)/ He
582 Thermochronology and Zircon Radiation Damage in the South American Passive Margin :
583 Thermal Overprint of the Paraná LIP ? *Tectonics*, 37, 1–18.
- 584 Huhma, H., Kontinen, A., Mikkola, P., Halkoaho, T., Hokkanen, T., et al. (2012a) Nd isotopic
585 evidence for Archaean crustal growth in Finland. *Special Paper of the Geological Survey of*
586 *Finland*, 54, 176–213.
- 587 Huhma, H., Mänttari, I., Peltonen, P., Kontinen, A., Halkoaho, T., et al. (2012b) The age of the
588 Archean greenstone belts in Finland. In P. Hölttä, Eds., *The Archean of the Karelia Province in*
589 *Finland. Special Paper 54. Geological Survey of Finland*, pp. 73–174.
- 590 Irmer, G. (1985) Zum Einfluß der Apparatefunktion auf die Bestimmung von Streuquerschnitten
591 und Lebensdauern aus optischen Phononenspektren. *Experimentelle Technik der Physik*, 33,
592 501–506.
- 593 Johnson, J.E., Flowers, R.M., Baird, G.B. and Mahan, K.H. (2017) "Inverted" zircon and apatite
594 (U-Th)/He dates from the Front Range, Colorado: High damage zircon as a low-temperature
595 (<50°C) thermochronometer. *Earth and Planetary Science Letters*, 466, 80–90.
- 596 Kähkönen, Y. (2005) Svecofennian supracrustal rocks. In M. Lehtinen, P.A. Nurmi and O.T.
597 Rämö, Eds., *Precambrian geology of Finland - Key to the evolution of the Fennoscandian shield.*
598 *Developments in Precambrian Geology 14. Elsevier. Chap. 8, pp. 343–405.*

- 599 K pyaho, A., Moln r, F., Sorjonen-Ward, P., M ntt ri, I., Sakellaris, G. and Whitehouse, M.
600 (2016) New U-Pb age constraints for the timing of gold mineralization at the Pampalo gold
601 deposit, Archaean Hattu schist belt, eastern Finland, obtained from hydrothermally altered and
602 recrystallised zircon. *Precambrian Research*, 289, 48–61.
- 603 Klemme, S., Prowatke, S., M n er, C., Magee, C., Lahaye, Y., Zack, T., Kasemann, S., Cabato,
604 E. and Kaeser, B. (2008) Synthesis and preliminary characterization of new silicate, phosphate
605 and titanite reference glasses. *Geostandards and Geoanalytical Research*, 32, 39–54.
- 606 Kohn, B.P., Lorencak, M., Gleadow, A.J.W., Kohlmann, F., Raza, A., Osadetz, K.G. and
607 Sorjonen-Ward, P. (2009) A reappraisal of low-temperature thermochronology of the eastern
608 Fennoscandia Shield and radiation-enhanced apatite fission-track annealing. Geological Society,
609 London, Special Publications, 324, 193–216.
- 610 Kohn, B.P., Wagner, M.E., Lutz, T.M. and Organist, G. (1993) Anomalous Mesozoic thermal
611 regime, central Appalachian Piedmont: evidence from sphene and zircon fission-track dating.
612 *Journal of Geology*, 101, 779–794.
- 613 Kohonen, J. (2005) Sedimentary rocks, diabases, and late cratonic evolution. In M. Lehtinen,
614 P.A. Nurmi and O.T. R m , Eds., *Precambrian geology of Finland - Key to the evolution of the*
615 *Fennoscandian shield. Developments in Precambrian Geology 14*. Elsevier. Chap. 13, pp. 563–
616 603.
- 617 Koistinen, T., Stephens, M.B., Bogatchev, V., Nordgulen,  ., Wennerstr m, M. and Korhonen, J.
618 (2001) Geological map of the Fennoscandian Shield, scale 1:2 million. Geological Surveys of
619 Finland, Norway and Sweden and North-West Department of Natural Resources of Russia.

- 620 Kontinen, A., Paavola, J. and Lukkarinen, H. (1992) K-Ar ages of hornblende and biotite from
621 late Archaean rocks of eastern Finland - interpretation and discussion of tectonic implications.
622 Geological Survey of Finland, Bulletin, 365, 1–31.
- 623 Kraml, M., Pik, R., Rahn, M., Selbekk, R., Carignan, J. and Keller, J. (2006) A New Multi-
624 Mineral Age Reference Material for $^{40}\text{Ar}/(^{39}\text{Ar}, (\text{U-Th})/\text{He}$ and Fission Track Dating Methods:
625 The Limberg t3 Tuff. *Geostandards and Geoanalytical Research*, 30, 73–86.
- 626 Lahtinen, R., Korja, A. and Nironen, M. (2005) Paleoproterozoic tectonic evolution. In M.
627 Lehtinen, P.A. Nurmi and O.T. Rämö, Eds., *Precambrian geology of Finland - Key to the*
628 *evolution of the Fennoscandian shield. Developments in Precambrian Geology 14.* Elsevier.
629 Chap. 11, pp. 481–531.
- 630 Larson, S.Å., Tullborg, E.L., Cederbom, C. and Stiberg, J.P. (1999) Sveconorwegian and
631 Caledonian foreland basins in the Baltic Shield revealed by fission-track thermochronology.
632 *Terra Nova*, 11, 210–215.
- 633 Lehtovaara, J. (1976) Apatite fission track dating of Finnish Precambrian intrusives. *Annales*
634 *Academiae Scientiarum Fennicae*, 117, 1–94.
- 635 Lenz, C., Nasdala, L., Talla, D., Hauzenberger, C., Seitz, R. and Kolitsch, U. (2015) Laser-
636 induced REE³⁺ photoluminescence of selected accessory minerals - An "advantageous artefact"
637 in Raman spectroscopy. *Chemical Geology*, 415, 1–16.
- 638 Lorencak, M. (2003) Low temperature thermochronology of the Canadian and Fennoscandian
639 Shields. PhD thesis. University of Melbourne, p. 300.

- 640 Lucassen, F., Franz, G., Dulski, P., Romer, R.L. and Rhede, D. (2011) Element and Sr isotope
641 signatures of titanite as indicator of variable fluid composition in hydrated eclogite. *Lithos*, 121,
642 12–24.
- 643 Lumpkin, G.R. (2006) Ceramic waste forms for actinides. *Elements*, 2, 365–372.
- 644 Lumpkin, G.R., Eby, R.K. and Ewing, R.C. (1991) Alpha-recoil damage in titanite (CaTiSiO₅):
645 direct observation and annealing study using high resolution transmission electron microscopy.
646 *Journal of Materials Research*, 6, 560–564.
- 647 Lünsdorf, N.K. and L nsdorf, J.O. (2016) Evaluating Raman spectra of carbonaceous matter by
648 automated, iterative curve-fitting. *International Journal of Coal Geology*, 160-161, 51–62.
- 649 Meyer, H.W., Zhang, M., Bismayer, U., Salje, E.K.H., Schmidt, C., Kek, S., Morgenroth, W. and
650 Bleser, T. (1996) Phase transformation of natural titanite: An infrared, Raman spectroscopic,
651 optical birefringence and X-ray diffraction study. *Phase Transitions*, 59, 39–60.
- 652 Mikkola, P., Heilimo, E., Paavola, J., Halkoaho, T., Äikäs, O. and Huhma, H. (2013) Lentuan
653 kompleksin eteläosan kallioperä. Summary: Bedrock of the southern part of the Lentua complex.
654 Tutkimusraportti - Report of Investigation, 202, 96.
- 655 Molnár, F., O'Brien, H., Lahaye, Y., Kapyaho, A. and Sakellaris, G. (2016) Signatures of
656 Multiple Mineralization Processes in the Archean Orogenic Gold Deposit of the Pampalo Mine,
657 Hattu Schist Belt, Eastern Finland. *Economic Geology*, 111, 1659–1703.
- 658 Molnár, K. (2018) Eruption chronology of the Ciomadul volcanic complex based on zircon (U-
659 Th)/He geochronology. Unpublished PhD thesis. Eötvös University, Budapest.
- 660 Murrell, G.R. (2003) The long-term thermal evolution of central Fennoscandia, revealed by low-
661 temperature thermochronometry. PhD thesis. Vrije Universiteit Amsterdam, p. 219.

- 662 Murrell, G.R. and Andriessen, P.A.M. (2004) Unravelling a long-term multi-event thermal record
663 in the cratonic interior of southern Finland through apatite fission track thermochronology.
664 *Physics and Chemistry of the Earth*, 29, 695–706.
- 665 Naeser, C.W. and Forbes, R.B. (1976) Variation of fission track ages with depth in two deep drill
666 holes. *Eos, Transactions American Geophysical Union*, 57, 353.
- 667 Nasdala, L., Reiners, P.W., Garver, J.I., Kennedy, A.K., Stern, R.A., Balan, E. and Wirth, R.
668 (2004) Incomplete retention of radiation damage in zircon from Sri Lanka. *American*
669 *Mineralogist*, 89, 219–231.
- 670 Nasdala, L., Wenzel, M., Vavra, G., Irmer, G., Wenzel, T. and Kober, B. (2001) Metamictisation
671 of natural zircon: accumulation versus thermal annealing of radioactivity-induced damage.
672 *Contributions to Mineralogy and Petrology*, 141, 125–144.
- 673 Nurmi, P.A., Sorjonen-Ward, P. and Damstén, M. (1993) Geological setting, characteristics and
674 exploration history of the mesothermal gold occurrences in the late Archean Hattu schist belt,
675 Ilomantsi, eastern Finland. In P. Nurmi and P. Sorjonen-Ward, Eds., *Geological Development,*
676 *Gold Mineralization and Exploration Methods in the Late Archean Hattu Schist Belt, Ilomantsi,*
677 *Eastern Finland. Special Paper 17. Geological Survey of Finland, Espoo, pp. 193–231.*
- 678 O'Brien, H., Huhma, H. and Sorjonen-Ward, P. (1993) Petrogenesis of the Late Archean Hattu
679 schist belt, Ilomantsi, eastern Finland: Geochemistry and Sr, Nd isotopic composition. In P.A.
680 Nurmi and P. Sorjonen-Ward, Eds., *Geological Development, Gold Mineralization and*
681 *Exploration Methods in the Late Archean Hattu Schist Belt, Ilomantsi, Eastern Finland. Special*
682 *Paper 17. Geological Survey of Finland, Espoo, pp. 147–184.*

- 683 Orme, D.A., Guenther, W.R., Laskowski, A.K. and Reiners, P.W. (2016) Longterm
684 tectonothermal history of Laramide basement from zircon–He age–eU correlations. Earth and
685 Planetary Science Letters, 453, 119–130.
- 686 Palenik, C.S., Nasdala, L. and Ewing, R.C. (2003) Radiation damage in zircon. American
687 Mineralogist, 88, 770–781.
- 688 Pidgeon, R.T. (2014) Zircon radiation damage ages. Chemical Geology, 367, 13–22.
- 689 Puura, V., Amantov, A., Tikhomirov, S. and Laitakari, I. (1996) Latest events affecting the
690 Precambrian basement, Gulf of Finland and surrounding areas. Special Paper of the Geological
691 Survey of Finland, 21, 115–125.
- 692 Reiners, P.W. (2005) Zircon (U–Th)/He Thermochronometry. Reviews in Mineralogy and
693 Geochemistry, 58, 151–179.
- 694 Reiners, P.W. and Farley, K.A. (1999) Helium diffusion and (U–Th)/He thermochronometry of
695 titanite. Geochimica et Cosmochimica Acta, 63, 3845–3859.
- 696 Salje, E.K.H., Schmidt, C. and Bismayer, U. (1993) Structural phase transition in titanite,
697 CaTiSiO₅: A ramanspectroscopic study. Physics and Chemistry of Minerals, 19, 502–506.
- 698 Salje, E.K.H., Taylor, R.D., Safarik, D.J., Lashley, J.C., Groat, L.A., Bismayer, U., James Evans,
699 R. and Friedman, R. (2012) Evidence for direct impact damage in metamict titanite CaTiSiO₅.
700 Journal of physics. Condensed matter : an Institute of Physics journal, 24, 052202.
- 701 Salje, E.K., Safarik, D.J., Lashley, J.C., Groat, L.A. and Bismayer, U. (2011) Elastic softening of
702 metamict titanite CaTiSiO₅: Radiation damage and annealing. American Mineralogist, 96, 1254–
703 1261.

- 704 Sarapää, O. (1996) Proterozoic primary kaolin deposits at Virtasalmi, south-eastern Finland. PhD
705 thesis, p. 169.
- 706 Schoene, B., Schaltegger, U., Brack, P., Latkoczy, C., Stracke, A. and Günther, D. (2012) Rates
707 of magma differentiation and emplacement in a ballooning pluton recorded by U-Pb TIMS-TEA,
708 Adamello batholith, Italy. *Earth and Planetary Science Letters*, 355-356, 162–173.
- 709 Shuster, D.L., Flowers, R.M. and Farley, K.A. (2006) The influence of natural radiation damage
710 on helium diffusion kinetics in apatite. *Earth and Planetary Science Letters*, 249, 148–161.
- 711 Sliupa, S., Fokin, P.A., Lazauskiene, J. and Stephenson, R.A. (2006) The Vendian-Early
712 Palaeozoic sedimentary basins of the East European Craton. In D.G. Gee and R.A. Stephenson,
713 Eds., *European Lithosphere Dynamics*. Vol. 32. *Memoirs. Geological Society London*, London,
714 pp. 449–462.
- 715 Sorjonen-Ward, P., Hartikainen, A., Nurmi, P., Rasilainen, K., Schaub, P., Zhang, Y. and
716 Liikanen, J. (2015) Exploration Targeting and Geological Context of Gold Mineralization in the
717 Neoproterozoic Ilimaussaq Greenstone Belt in Eastern Finland. In W.D. Maier, R. Lahtinen and H.
718 O'Brien, Eds., *Mineral Deposits of Finland*. Elsevier. Chap. 5.3, pp. 435–466.
- 719 Sorjonen-Ward, P. (1993) An overview of structural evolution and lithic units within and
720 intruding the late Archean Hattu schist belt, Ilimaussaq, eastern Finland. In P.A. Nurmi and P.
721 Sorjonen-Ward, Eds., *Geological development, gold mineralization and exploration methods in*
722 *the late Archean Hattu schist belt, Ilimaussaq, eastern Finland*. Special Paper 17. *Geological*
723 *Survey of Finland*, Espoo, pp. 9–102.
- 724 Sorjonen-Ward, P. and Clauqué-Long, J. (1993) A preliminary note on ion probe results for
725 zircons from the Silvevaara Granodiorite, Ilimaussaq, eastern Finland. In S. Autio, Eds.,

- 726 Geological Survey of Finland, Current Research 1991-1992. Special Paper 18. Geological Survey
727 of Finland, pp. 25–29.
- 728 Speer, J.A. and Gibbs, G.V. (1976) The crystal structure of synthetic titanite, CaTiOSiO_4 , and
729 the domain textures of natural titanites. *American Mineralogist*, 61, 238–247.
- 730 Stefanovsky, S.V., Yudintsev, S.V., Giere, R. and Lumpkin, G.R. (2004) Nuclear waste forms. In
731 R. Gieré and P. Stille, Eds., *Energy, Waste and the Environment: a Geochemical Perspective*.
732 Special Publications 236. Geological Society London, pp. 37–63.
- 733 Stockli, D.F. and Farley, K.A. (2004) Empirical constraints on the titanite (UTh)/ He partial
734 retention zone from the KTB drill hole. *Chemical Geology*, 207, 223–236.
- 735 Tiepolo, M., Oberti, R. and Vannucci, R. (2002) Trace-element incorporation in titanite:
736 Constraints from experimentally determined solid/liquid partition coefficients. *Chemical*
737 *Geology*, 191, 105–119.
- 738 Vaasjoki, M., Sorjonen-Ward, P. and Lavikainen, S. (1993) U-Pb age determinations and sulfide
739 Pb-Pb characteristics from the late Archean Hattu schist belt, Ilomantsi, eastern Finland. In P.A.
740 Nurmi and P. Sorjonen-Ward, Eds., *Geological development, gold mineralization and exploration*
741 *methods in the late Archean Hattu schist belt, Ilomantsi, eastern Finland*. Special Paper 17.
742 Geological Survey of Finland, Espoo, pp. 103–131.
- 743 Weber, W.J., Ewing, R.C., Catlow, C.R.A., Hobbs, L.W., Kinoshita, C., Motta, A.T., Nastasi, M.
744 and Salje, E.K.H. (1998) Radiation effects in crystalline ceramics for the immobilization of high-
745 level nuclear waste and plutonium. *Journal of Materials Research*, 13.
- 746 Wojdyr, M. (2010) Fityk: a general-purpose peak fitting program. *Journal of Applied*
747 *Crystallography*, 43, 1126–1128.

- 748 Wolf, R.A., Farley, K.A. and Silver, L.T. (1996) Helium diffusion and low-temperature
749 thermochronometry. *Planetary Sciences*, 60, 4231–4240.
- 750 Xu, L., Bi, X., Hu, R., Tang, Y., Wang, X. and Xu, Y. (2015) LA-ICP-MS mineral chemistry of
751 titanite and the geological implications for exploration of porphyry Cu deposits in the Jinshajiang
752 - Red River alkaline igneous belt, SW China. *Mineralogy and Petrology*, 109, 181–200.
- 753 Zeitler, P.K., Herczeg, A.L., McDougall, I. and Honda, M. (1987) U-Th-He dating of apatite: A
754 potential thermochronometer. *Geochimica et Cosmochimica Acta*, 51, 2865–2868.
- 755 Zeitler, P.K. (2015) U-Th/He Dating. In J.W. Rink and J.W. Thompson, Eds., *Encyclopedia of*
756 *Scientific Dating Methods*. Springer, pp. 932–940.
- 757 Zhang, M. and Salje, E.K.H. (2003) Spectroscopic characterization of metamictization and
758 recrystallization in zircon and titanite. *Phase Transitions*, 76, 117–136.
- 759 Zhang, M., Salje, E.K.H., Farnan, I., Graeme-Barber, A., Daniel, P., Ewing, R.C., Clark, A.M.
760 and Leroux, H. (2000) Metamictization of zircon: Raman spectroscopic study. *Journal of*
761 *Physics: Condensed Matter*, 12, 1915–1925.
- 762 Zhang, M., Salje, E.K.H., Redfern, S.A.T., Bismayer, U. and Groat, L.A. (2013) Intermediate
763 structures in radiation damaged titanite (CaTiSiO₅): a Raman spectroscopic study. *Journal of*
764 *physics. Condensed matter : an Institute of Physics journal*, 25, 12.

765 **Appendices**

- 766 Data Repository for "Estimation of radiation damage in titanites using Raman spectroscopy"
767 The material in this data repository containing 5 Tables, one figure and one zip-file includes
768 information on:

769 Appendix 1: Used IFORS configuration files (14) and one overview table. (Appendix-
770 3_IFORS_config_files.zip)

771 Appendix 2: Alpha-emitting element contents of the samples and compilation of mean peak
772 values generated by the evaluation of the entire spectra. Table shows all results of the 14 different
773 settings applied (see explanation in text and Appendix 1). (Appendix-
774 2_Compil_damage_and_Raman_entire_evaluation_all_settings.xls)

775 Appendix 3: Peak width and position values of the band 465 cm⁻¹ using setting wf_sm (see
776 details in Appendix 1). (Appendix-3_Single-band-evaluation_465.xls)

777 Appendix 4: Peak width and position values of the band 424 cm⁻¹ using setting wf_sm (see
778 details in Appendix 1). (Appendix-4_Single-band-evaluation_424.xls)

779 Appendix 5: Plot of (unweighted) mean FWHMs versus α -dose for 3 different curve-fitting
780 protocols (Appendix-5_meanfwhm-alphadose.pdf).

781 Appendix 6: Regression line parameters for all curve-fitting protocols for different damage
782 accumulation durations (plots presented in Figure 5). (Appendix-
783 6_Regression_line_parameters.xls)

784 Appendix 7: (U-Th)/He age data (Appendix-7_The_ages.xls)

785 **Figure captions**

786 Figure 1: Two Raman spectra of titanite crystals with different α -doses (a: 1.3×10^{13} α /g and b:
787 1.25×10^{18} α /g). The spectra were evaluated with the software IFORS (Lünsdorf and Lünsdorf
788 2016). The black lines are the spectrum data, which are mostly covered by the dashed green lines
789 representing fitted data, blue dashed lines are the calculated background correction and thin red

790 lines are the respective pseudo-Voigt functions. The black numbers give the positions of the
791 important bands in cm^{-1} .

792 Figure 2: (a): Geological overview of Fennoscandia, the black rectangle refers to the area in (b)
793 that shows the entire Iломантси-Kostomuksha greenstone belt. (c): Geological map of the
794 Iломантси greenstone belt (purple) with the sampling locations (orange circles) in the Karelian
795 domain of Fennoscandia (modified after Koistinen et al. 2001). The Iломантси greenstone belt
796 consist of the Hattu schist belt (purple polygon) and the Kovero belt (dashed purple polygon).

797 Figure 3: α -dose of the analyzed titanite grains versus the FWHMs of the 465 cm^{-1} band (a & b)
798 and the 424 cm^{-1} band (c & d). The linear and logarithmic plots show the same data, but the semi-
799 logarithmic presentation emphasizes better the onset of the significant changes in the crystal
800 lattice - which has prominent importance at helium thermochronology (see in Discussion). The
801 color of the points indicates the position of the center of the pV-functions. Only pV-functions
802 with an area greater than 1% of the total area and a $\text{FWHM} < 75 \text{ cm}^{-1}$ were considered. Black
803 continuous lines in the linear presentations (a) and (c) are linear regressions shown with 0.95
804 confidence intervals (grey belts). Their formulae are $\text{FWHM}[\text{cm}^{-1}] \sim 19.5(\pm 0.5)[\text{cm}^{-1}]$
805 $+ 1.42(\pm 0.06) \times 10^{-17}[\text{cm}^{-1}/(\alpha/\text{g})] \times \alpha\text{-dose}[\alpha/\text{g}]$, $R^2=0.52$ for the 465 cm^{-1} band (a) and
806 $\text{FWHM}[\text{cm}^{-1}] \sim 15.6(\pm 0.3)[\text{cm}^{-1}] + 1.30(\pm 0.03) \times 10^{-17}[\text{cm}^{-1}/(\alpha/\text{g})] \times \alpha\text{-dose}[\alpha/\text{g}]$, $R^2=0.69$ for the
807 424 cm^{-1} band (c). The dashed fit in (a) and (b) with $\text{FWHM}[\text{cm}^{-1}] \sim 16.9(\pm 0.3)[\text{cm}^{-1}]$
808 $+ 1.83(\pm 0.07) \times 10^{-17}[\text{cm}^{-1}/(\alpha/\text{g})] \times \alpha\text{-dose}[\alpha/\text{g}]$, $R^2=0.61$ was calculated for all samples with
809 $\text{FWHM} < 40 \text{ cm}^{-1}$ and damage density $< 1 \times 10^{18} \alpha/\text{g}$ and is more adequate for the low-damage
810 range. The grey dashed vertical lines in (b) and (d) correspond to $5 \times 10^{16} \alpha/\text{g}$ and $5 \times 10^{17} \alpha/\text{g}$.
811 For data see Appendices 5 and 6.

812 Figure 4: Intensity weighted mean FWHMs (iw-FWHM) versus the α -dose in linear (a) and
813 semi-logarithmic (b) scale for two curve-fitting protocols, *wf_sm* allowing up to 40 pV-
814 functions and *wf_sm_max15* allowing up to 15 pV-functions. Black continuous lines correspond
815 to the linear regression calculated over both datasets, shown in (a) with 0.95 confidence interval
816 (grey belt). The formula is $\text{iw-FWHM}[\text{cm}^{-1}] \sim 39.3(\pm 0.8)[\text{cm}^{-1}] + 3.89(\pm 0.09) \times 10^{-17}[\text{cm}^{-1}$
817 $^{1/(\alpha/\text{g})}] \times \alpha\text{-dose}[\alpha/\text{g}]$, $R^2=0.75$. The dashed lines indicate the possible threshold values of
818 $5 \times 10^{16} \alpha/\text{g}$ (this study) and $5 \times 10^{17} \alpha/\text{g}$ [2]. Both setups show the same trend which is flat below
819 $5 \times 10^{16} \alpha/\text{g}$ and linear above this value. For fitting details see Appendix 1.

820 Figure 5: (a) Summary of the results of the different fitting methods. The axes represent the linear
821 regression parameters of the FWHM vs. α -dose correlations. Symbol shapes refer to calculation
822 method; big symbols are curve-fitting protocols with automated background correction, small
823 symbols are protocols with manual background correction. The color coding gives the coefficient
824 of determination of the linear regressions, the blue lines contour the density distribution. All
825 linear regression parameters for each setting can be found in Appendix 5. The generally higher
826 values for weighted means compared to unweighted means and medians are due to the intensity
827 and area weighting. The tightest distribution was generated by the intensity weighted mean
828 FWHMs (iw-FHWM), which yielded very similar results for all different settings, show
829 consistently high R^2 and are thus considered the most robust calculation method. (b) shows the
830 linear regression parameters for only two of the curve-fit protocols, *wf_sm* (open symbols)
831 allowing up to 40 pV-functions and *wf_sm_max15* (filled symbols) allowing up to 15 pV-
832 functions. Linear regressions were calculated for different α -damage accumulation durations
833 which are displayed in different colors. For the intensity weighted mean FWHM the two

834 protocols give very similar results. Lowering the α -damage accumulation duration by 0.1 Gyr
835 increases the slope values by ~ 7 – 8% .

836 Figure 6: Titanite (U–Th)/He ages in relation to their α -dose, eU contents and the intensity
837 weighted mean FWHM (iw-FHWM) of the corresponding Raman spectra. (a) Titanite (U–
838 Th)/He (THE) ages versus their α -dose, color indicates the eU contents. (b) Relation of the THE
839 ages vs. iw-FHWM. The color indicates the α -dose. The observed dispersion is mainly due to the
840 rather poor THE age vs. eU correlation of our dataset.

Table 1: Locality, lithology and emplacement age of the studied titanite-bearing formations from Finland.

Sample	YKJ-north ¹	YKJ-east ¹	Location	Rock type	Zircon U-Pb Age [Ma] (±2s)	Titanite U-Pb Age [Ma] (±2s)	Reference
A0050	6958398	3702479	Ilomantsi Kk	Granodiorite (sanukitoid)	2728 (7)	2707 (10)	Vaasjoki et al. 1993; Heilimo et al., 2011
A0284	6973076	3710317	Lehtovaara Ilomantsi	Granodiorite	2752 (4)	2705 (10)	Sorjonen-Ward & Claoue-Long, 1993; Vaasjoki et al 1993
A0301	6968216	3697164	Vehkavaara Ilomantsi	Porphyry (felsic, dyke)	2755 (4)	2720 (10)	Vaasjoki et al., 1993; Huhma et al., 2012a
A0338	6968216	3697164	Vehkavaara Ilomantsi	Porphyry (felsic, dyke)		2747 (15)	Vaasjoki et al., 1993
A0339	6983951	3706826	Silvevaara Ilomantsi	Granodiorite (porphyritic)		2658 (10)	Vaasjoki et al., 1993
A0357	6945820	3530110	Paukarlahti	Gneiss (granitic, dome)		1824 (10)	Gaal, 1980
A0804	6982475	3586352	Luikonlahti Kaavi	Granite			
A0951	6946074	3696122	Paavonvaara Ilomantsi	Granite			
A1078	6953174	3715702	Oinassalmi Ilomantsi	Diorite (quartz-, sanukitoid)	2744 (3)		Vaasjoki et al., 1993; Heilimo et al., 2011
A1095	6974229	3713990	Kivisuo Ilomantsi	Porphyry (Qtz-Fldsp)	2756 (6)		Vaasjoki et al., 1993
A1340	7003399	3669913	Jaakonvaara Lieksa	Diorite	2702 (5)		Halla, 2002; Mikkola et al., 2013
A1614	7003710	3542680	Pajulahti Nilsiä	Syenite			
A1626	6944376	3674468	Rasisuo	Gabbro	2756 (4)		Huhma et al., 2012a
A1640	6928741	3675065	Huhtilampi	Granite			
A1641	7009265	3711422	Kierrosaho	Granite (microcline)			
A1762	7027497	3661337	Emonvaara	Tonalite		2732 (15) ²	Huhma et al., 2012b
A1963	6959880	3708970	Kuikanniemi Ilomantsi	Granodiorite			
A1964	7021049	3685422	Kitsi	Granite			
A2196	6992639	3718302	Viluvaara	Granodiorite	2751 (4)	2737 (15)	Käpyaho et al., 2016

¹: Finnish national grid.

²:WR Sm-Nd age

Sheet1

Table 2: Sources and major parameters of the selected titanite reference samples having low radiation damage densities.

Sample	Locality	Source	U-Pb Age [Ma]
ECS	Ecstall pluton, British Columbia	Butler et al. (2002)	91.5
94T	U-Pb reference material; Univ. Arizona	from George Gehrels	51.5
ADA-15	Adamello massif, S. Alps	Schoene et al. (2012)	41.2 ¹
LIM	Kaiserstuhl ash, Rhine valley	Kraml et al. (2006)	16.5
MK-221b	Csomád volcano, Carpathians	Molnár (2018)	0.14
MK-5	Csomád volcano, Carpathians	Harangi et al. (2015)	0.03

¹: 20 Ma considered as cooling age and used for α -dose calculation (Heberer et al. 2017).

IFORS_tested_parameters

Table 3: Table of (preliminary) tested values for IFORS automated curve-fitting procedure. For detailed description of the parameters see Lünsdorf and Lünsdorf (2016), for used curve-fitting protocols see Appendix 1.

Parameter	tested values	function of parameter
start_wn	100	Specifies the start wavenumber (Raman shift) of the spectrum
stop_wn	1300, 1800	Specifies the stop wavenumber (Raman shift) of the spectrum
repetitions	1, 3	Sets the number repetitions / determines how often the spectrum is repeatedly evaluated
smoothing	yes, no	If set to 'yes', smoothing is enabled and the spectrum will be convoluted with a Hanning-Window filter
smoothing_size	9	Controls the window size of the Hanning-Window used for smoothing
min_width	1, 2	Controls the minimum half width at half maximum (HWHM) of the pseudo-Voigt functions during curve-fitting
max_width	50, 80, 100, 150	Controls the maximum half width at half maximum (HWHM) of the pseudo-Voigt functions during curve-fitting
min_distance	2, 5, 8, 10	Controls the minimum distance between two pseudo-Voigt functions during curve-fitting
baseline mode	window_filter, off	Style of baseline approximation. If set to 'window_filter', the baseline is approximated by a convolution of the baseline-data with a moving Hanning-window. If set to 'off' no baseline will be used during curve-fitting
window_size	0.25, 0.35	Sets the size of the Hanning-window used during baseline approximation when baseline_mode is set to 'window_filter'
noise_intensity	1-3.5	This parameter is a multiple of the standard deviation of the estimated noise distribution
max_peak_numb	10, 15, 20, 30, 35, 40	Sets the maximum number of pseudo-Voigt functions allowed during curve-fitting, e.g. if this number is reached the program stops
alpha	0.98	During curve-fitting, this parameter controls the width of the normal distribution from which the value is chosen that is added or subtracted from a randomly chosen pseudo-Voigt function parameter
sigma_threshold	0.01, 0.1, 0.5, 1	Controls the duration of the mutation-loop more directly. Legit values for 'sigma_threshold' are from the interval ' $2 > \text{sigma_threshold} > 0$ '. Values close to 2 result in short and values close to 0 in long mutation-loop duration

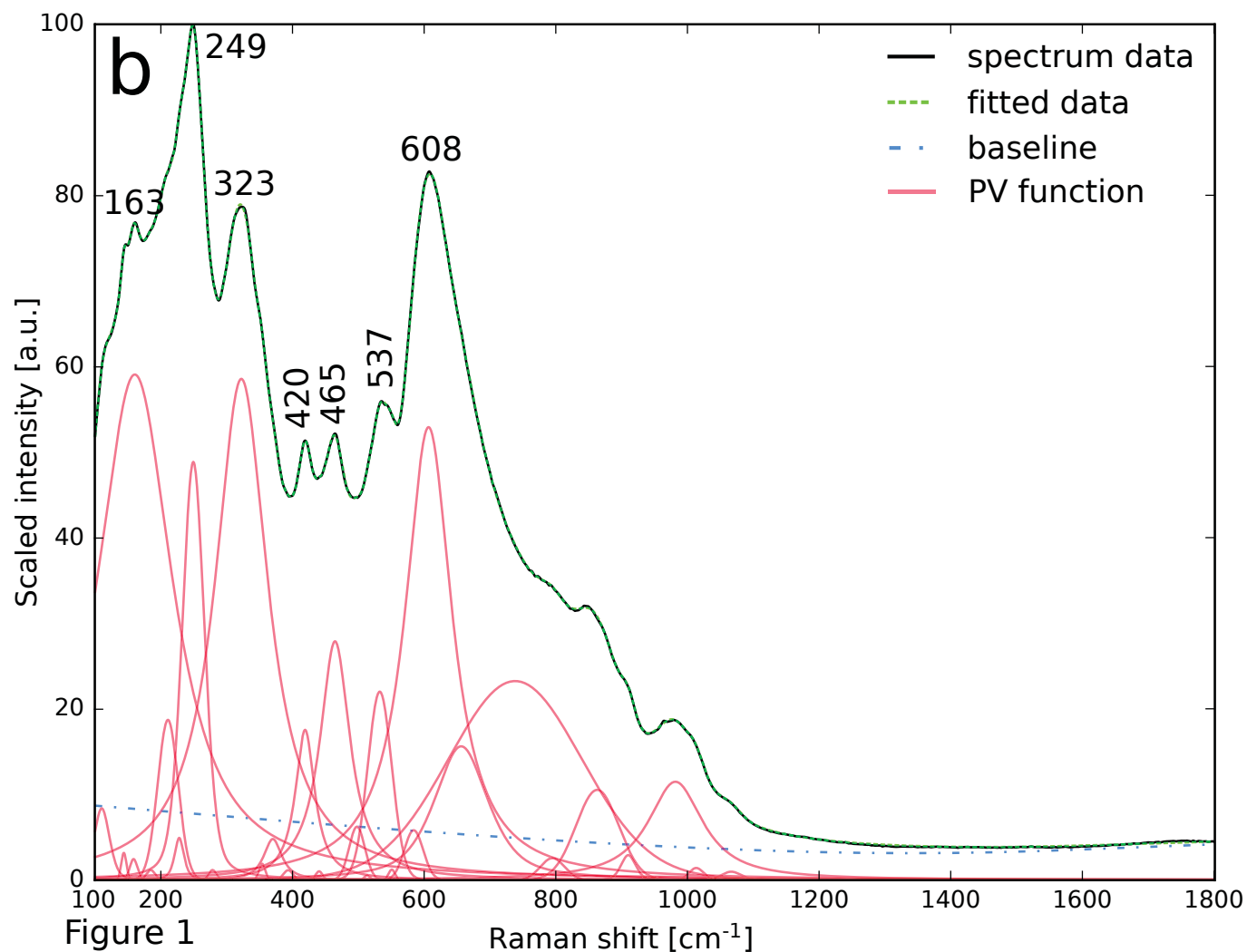
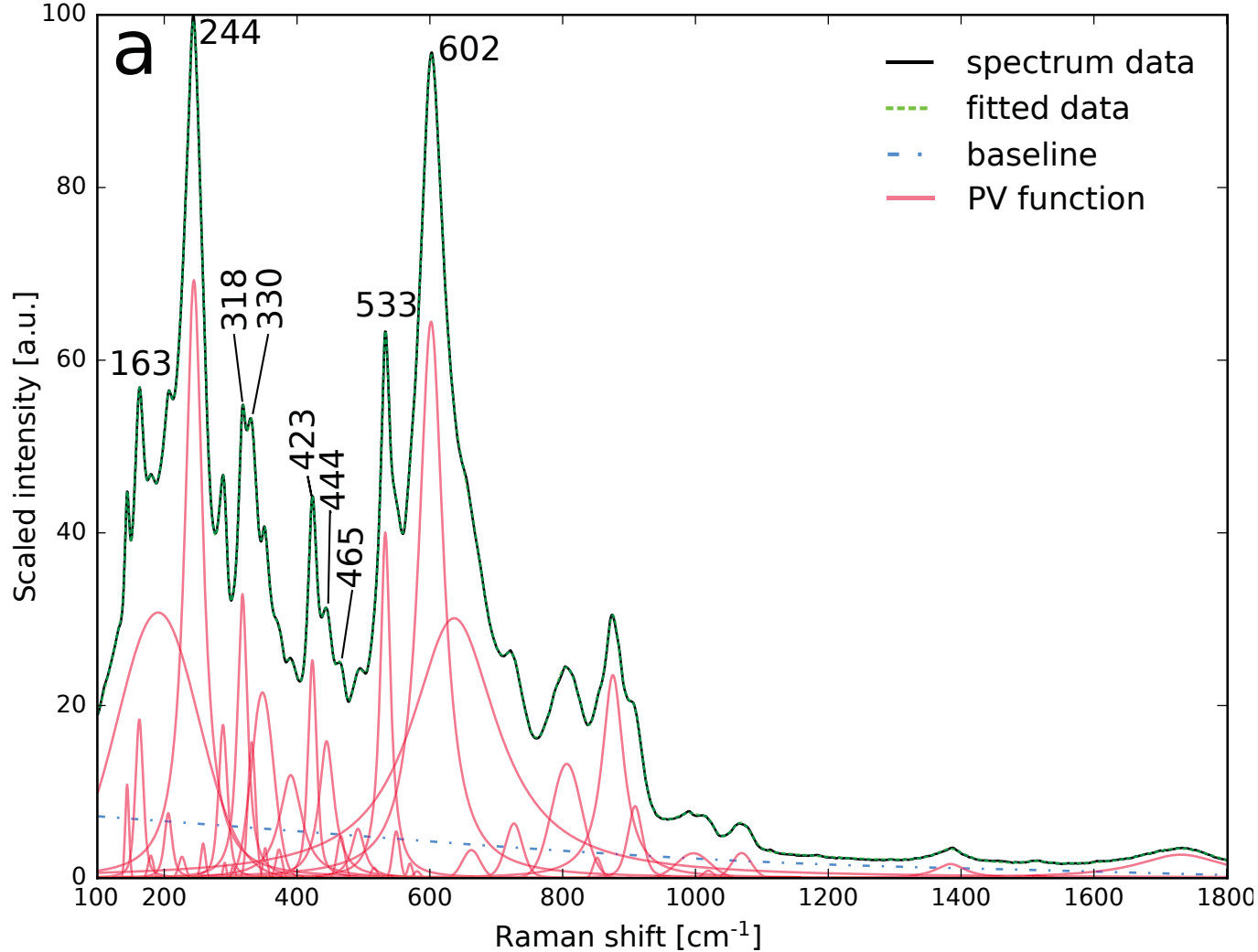


Figure 1

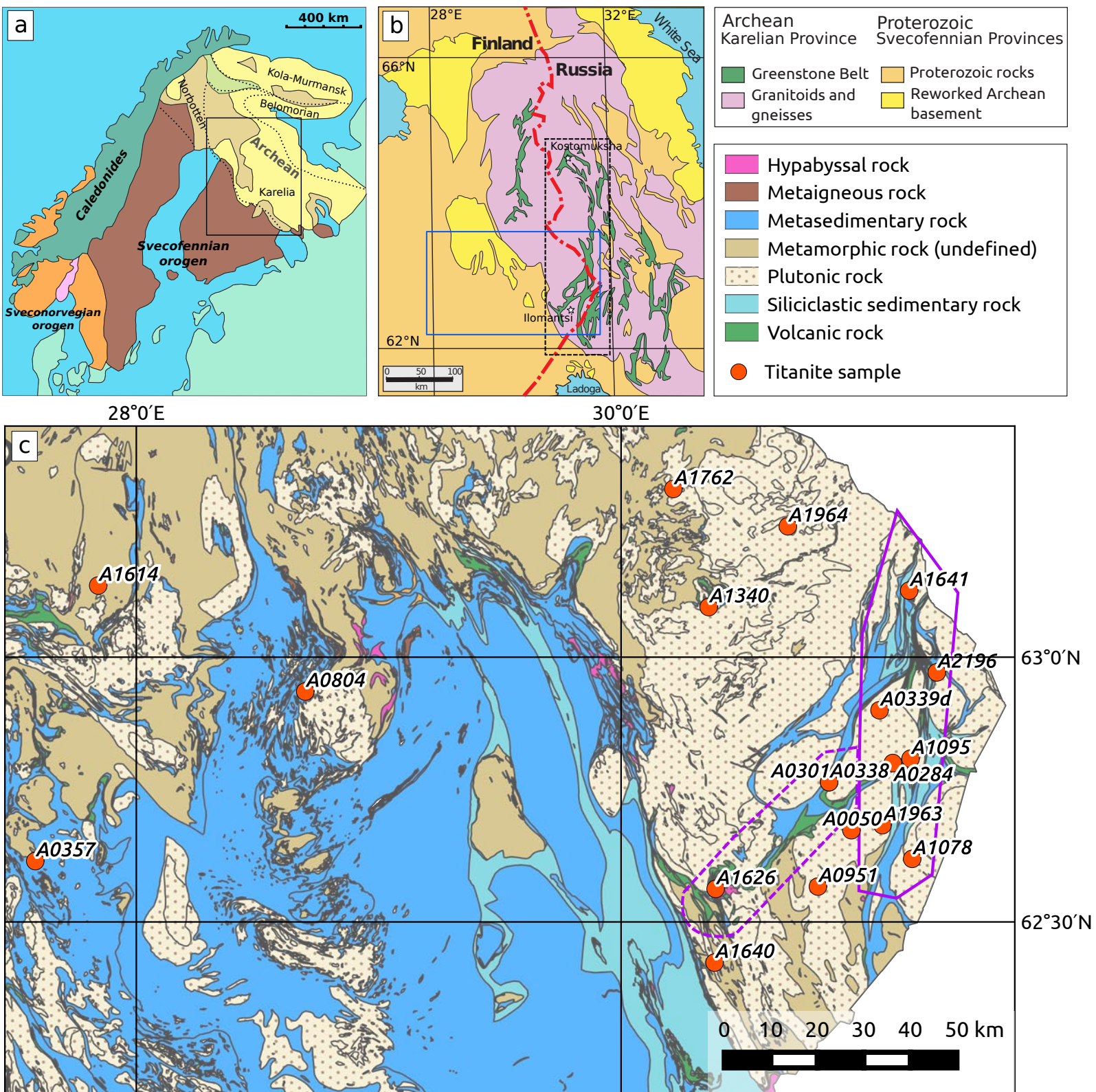


Figure 2

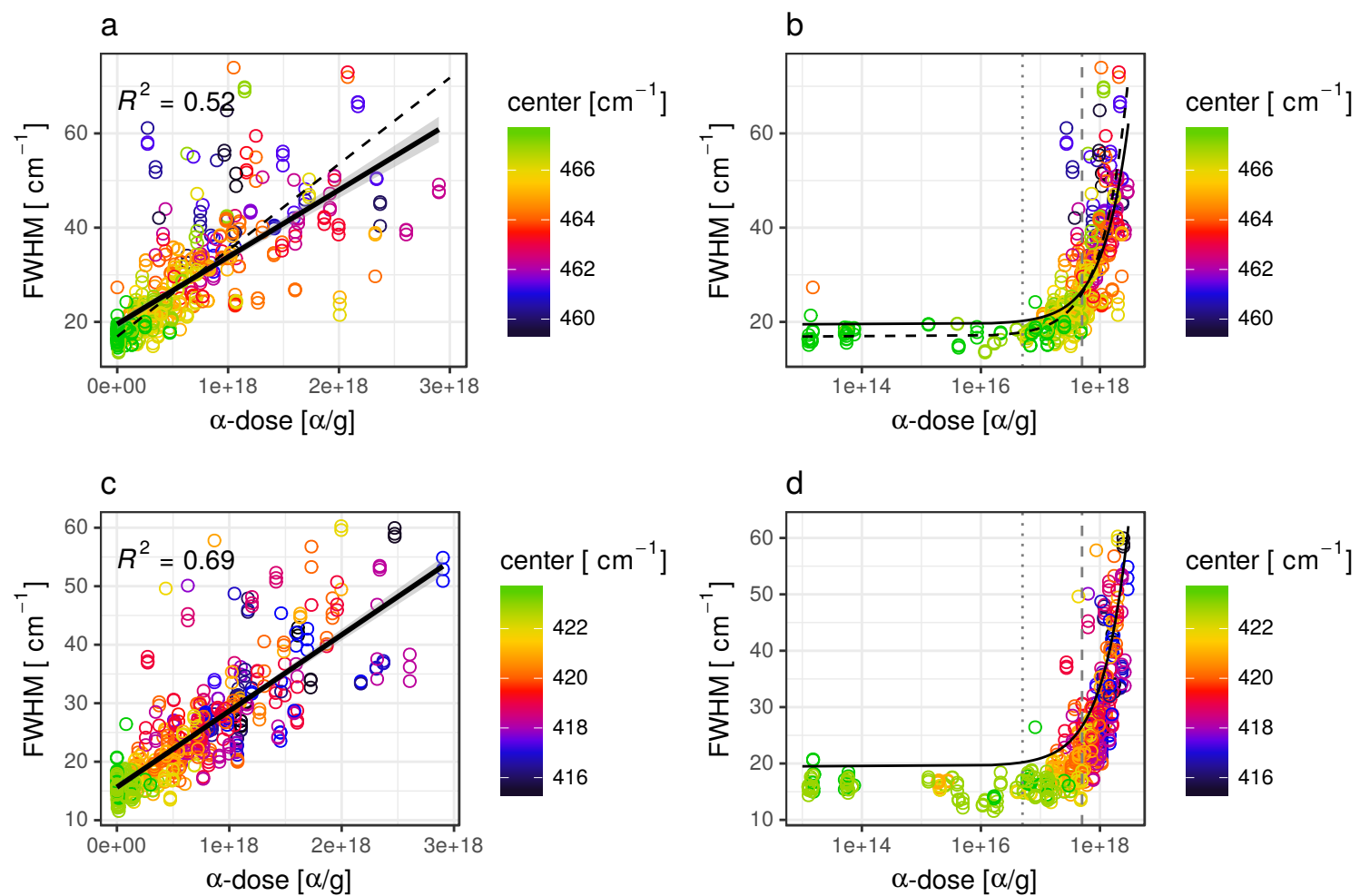


Figure3

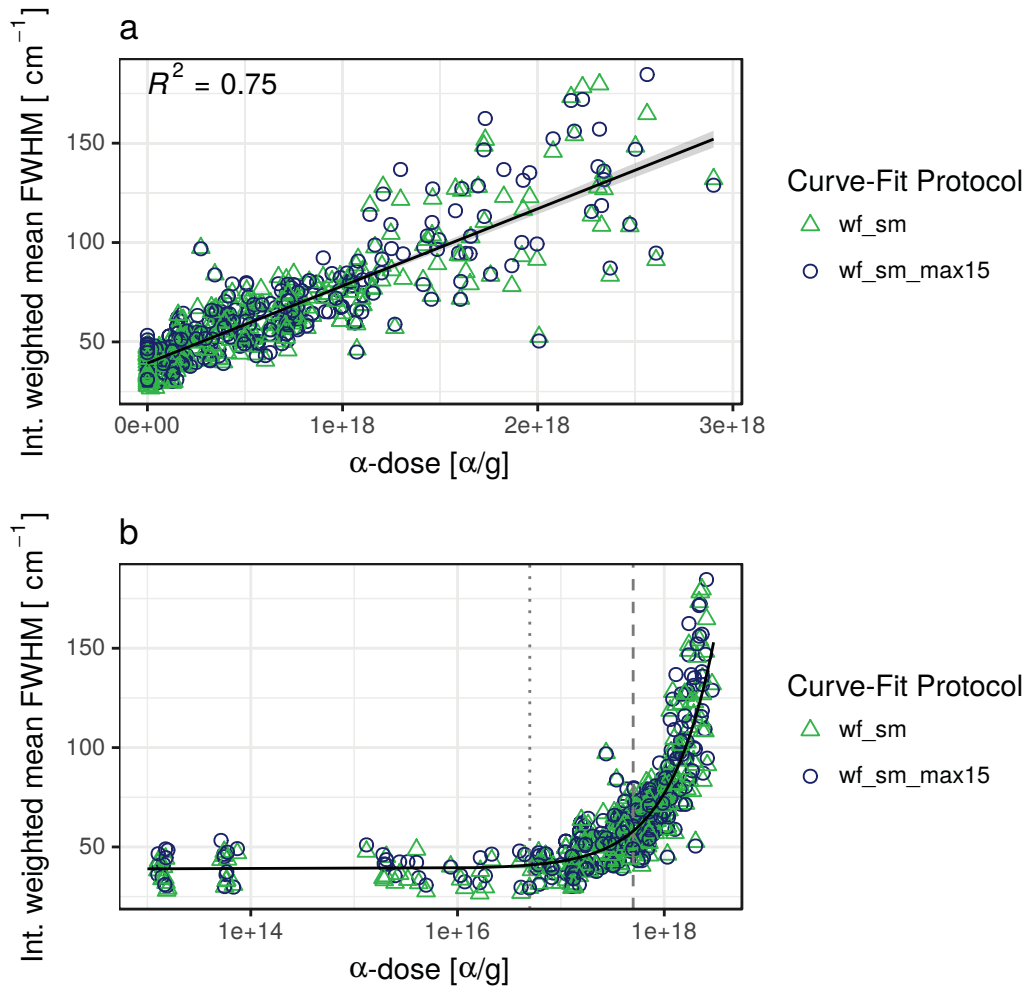


Figure4

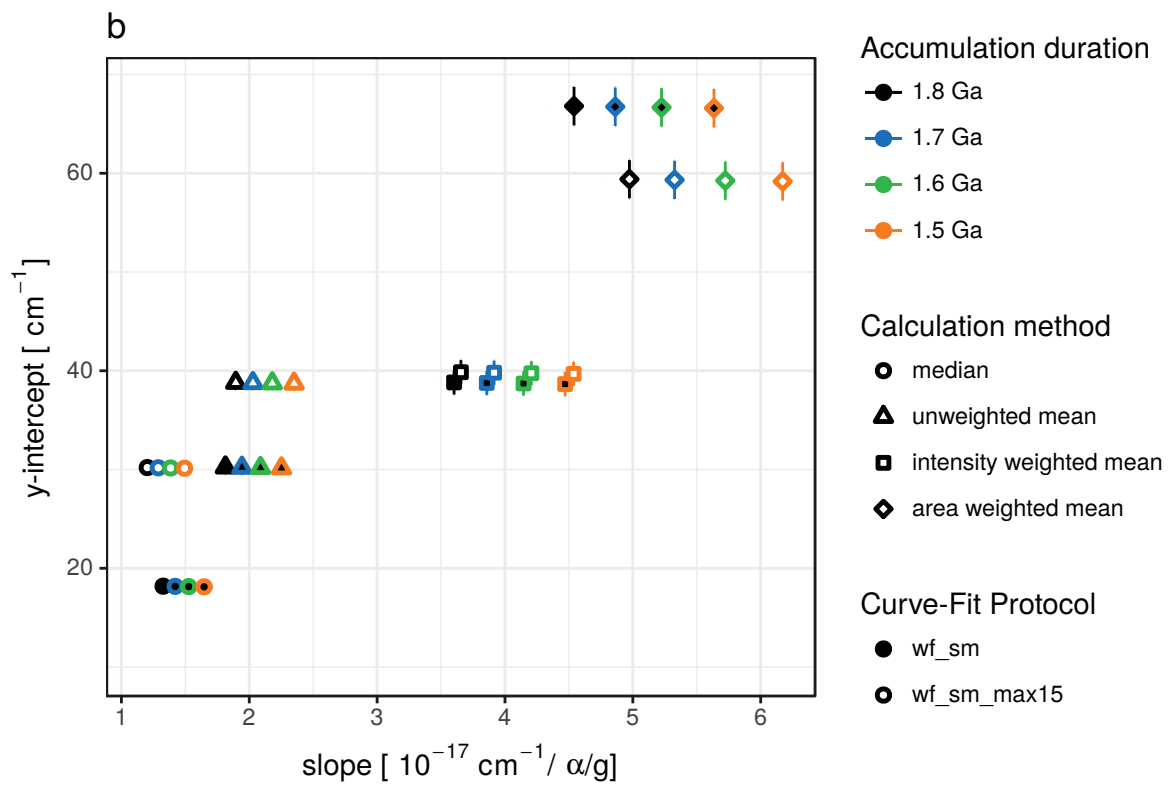
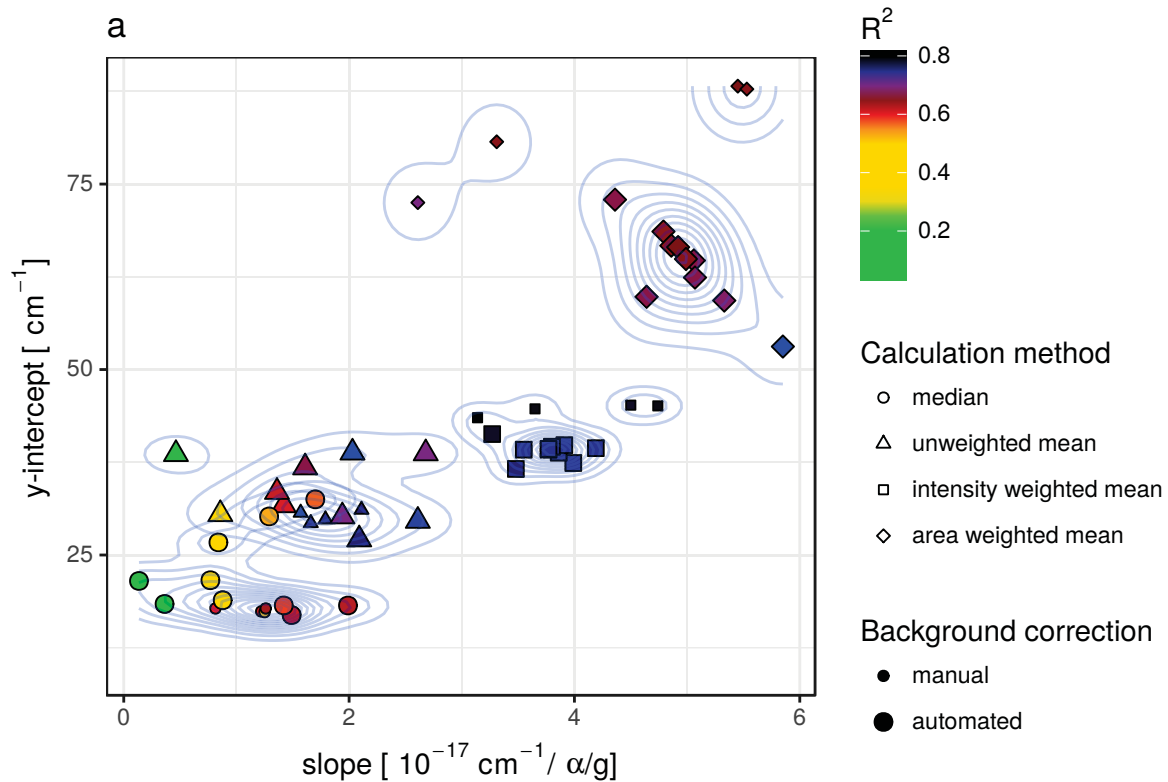


Figure5

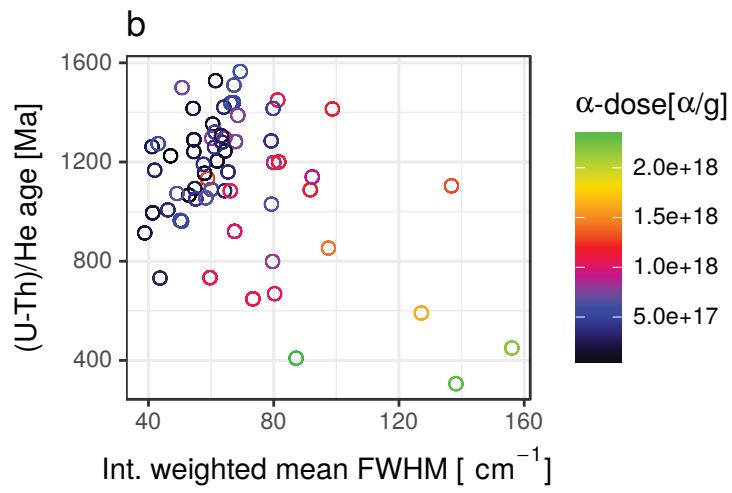
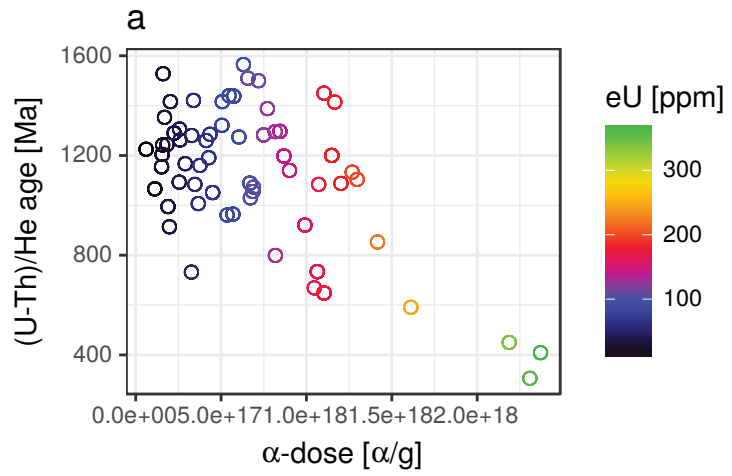


Figure6